

1 Untangling the solar wind and magnetospheric drivers of the radiation belt electrons

2 Simon Wing<sup>1</sup>, Jay R. Johnson<sup>2</sup>, Drew L. Turner<sup>1</sup>, Aleksandr Y. Ukhorskiy<sup>1</sup>, and  
3 Alexander J. Boyd<sup>3</sup>  
4

5 <sup>1</sup>The Johns Hopkins University, Applied Physics Laboratory, Laurel, Maryland, USA

6 <sup>2</sup>Andrews University, Berrien Spring, Michigan, USA

7 <sup>3</sup>The Aerospace Corporation, El Segundo, California, USA  
8

9 **Abstract.** Many solar wind parameters correlate with one another, which complicates the causal-  
10 effect studies of solar wind driving of the magnetosphere. Conditional mutual information (CMI)  
11 is used to untangle and isolate the effect of individual solar wind and magnetospheric drivers of  
12 the radiation belt electrons. The solar wind density ( $n_{sw}$ ) negatively correlates with electron phase  
13 space density (PSD) (average energy  $\sim 1.6$  MeV) with time lag ( $\tau$ ) = 15 hr. This effect of  $n_{sw}$  on  
14 PSD has been attributed to magnetopause shadowing losses, but when the effect of solar wind  
15 velocity ( $V_{sw}$ ) is removed,  $\tau$  shifts to 7–11 hr, which is a more accurate time scale for this process.  
16 The peak correlation between  $V_{sw}$  and PSD shifts from  $\tau = 38$  to 46 hr, when the effect of  $n_{sw}$  is  
17 removed. This suggests that the time scale for electron acceleration to 1–2 MeV is about 46 hr  
18 following  $V_{sw}$  enhancements. The effect of  $n_{sw}$  is significant only at  $L^* = 4.5$ –6 ( $L^* > 6$  is highly  
19 variable) whereas the effect of  $V_{sw}$  is significant only at  $L^* = 3.5$ –6.5. The peak response of PSD  
20 to  $V_{sw}$  is the shortest and most significant at  $L^* = 4.5$ –5.5. As time progresses, the peak response  
21 broadens and shifts to higher  $\tau$  at higher and lower  $L^*$ , consistent with local acceleration at  $L^* =$   
22 4.5–5.5 followed by outward and inward diffusion. The outward radial diffusion time scale at  $L^*$   
23 = 5–6 is  $\sim 40$  hr per  $R_E$ .

24  
25 ORCID ID: 0000-0001-9342-1813

26 **Plain Language Summary**

27 Many solar wind parameters correlate with one another, which complicates the causal-effect  
28 studies of solar wind driving of the magnetosphere. We use conditional mutual information (CMI),  
29 which is part of information theory, to untangle and isolate the effect of individual solar wind and  
30 magnetospheric drivers of the radiation belt electrons. For example, the solar wind density  
31 negatively correlates with electron phase space density (PSD) (average energy  $\sim 1.6$  MeV) with  
32 the response time lag of 15 hours. This has been attributed to the electron loss process called  
33 magnetopause shadowing. The time lag suggests the time scale for this process is 15 hours.  
34 However, when the effect of solar wind velocity is removed, the time lag is 7–11 hours, which is  
35 a more accurate time scale for this process. As another example, the time lag of the correlation  
36 between solar wind velocity and PSD shifts 38 to 46 hours, when the effect of solar wind density  
37 is removed. This suggests that the time scale for electron acceleration to 1–2 MeV is about 46  
38 hours following the solar wind velocity enhancements. We also show that the effects of solar wind  
39 velocity and density have dependence on radial distance.

40

41 **Keywords:** radiation belt, relativistic electrons, solar wind drivers, nonlinear relationships,  
42 information theory, local acceleration, diffusion time scale, electron acceleration, magnetopause  
43 shadowing.

44 **Index terms:** 2774, 2784, 2720, 2730, 4499

45 **Major science question:**

46 **New Science knowledge:**

47 **Broad Implications:** Information theoretical tools can be useful to untangle and isolate individual  
48 solar wind and magnetospheric drivers of the radiation belt.

49 **Key points:** (1) The effect of  $n_{sw}$  on radiation belt electrons is significant only at  $L^* = 4.5-6$  and  
50 not significant at  $L^* < 3$ . (2) The effect of  $V_{sw}$  on radiation belt electrons is significant at  $L^* =$   
51  $3.5-6.5$  and not significant at  $L^* < 3.5$ . (3) The radiation belt response time lag to  $V_{sw}$  suggests  
52 local acceleration at  $L^* = 4.5-5.5$  followed by outward and inward diffusion.

53

## 54 1. Introduction

55 The Earth's radiation belt is populated by electrons having energies of hundreds of keVs  
56 to  $>10$  MeVs. These electrons are hazardous to satellites that encounter them in the inner-  
57 magnetosphere  $r \sim 2-8 R_E$ , including at the geosynchronous orbit (GEO), and at their foot points at  
58 low earth orbit (LEO) in the ionosphere, where  $1 R_E =$  radius of the Earth = 6372 km. The MeV  
59 electrons can penetrate deep into spacecraft leading to spacecraft or instrument malfunctions while  
60 those with energies  $< 1$  MeV can accumulate on the surface of the spacecraft bodies, leading to  
61 electrical discharges.

62 It has long been recognized that the variabilities of the radiation belt electrons, to a large  
63 extent, are driven by the solar wind (e.g., *Baker et al.*, 2018; *Li et al.*, 2001; *Turner and Li*, 2008,  
64 *Reeves et al.*, 2013; *Xiang et al.*, 2017; *Pinto et al.*, 2018; *Zhao et al.*, 2017). However, many solar  
65 wind parameters positively and negatively correlate with one another, which can complicate the  
66 interpretation of the solar wind drivers of the radiation belt (e.g., *Wing et al.*, 2016; *Borovsky*,  
67 2018; 2020; *Maggiolo et al.*, 2017). For example, solar wind velocity ( $V_{sw}$ ) positively correlates  
68 with radiation belt electron fluxes ( $J_e$ ) (e.g., *Paulikas and Blake*, 1979; *Baker et al.*, 1990; *Reeves*  
69 *et al.*, 2011; *Balikhin et al.*, 2011; *Li et al.*, 2005; *Wing et al.*, 2016). Solar wind density ( $n_{sw}$ )  
70 negatively correlates with radiation belt  $J_e$  (e.g., *Li et al.*, 2005; *Lyatsky and Kazanov*, 2008;  
71 *Kellerman and Shprits*, 2012; *Rigler et al.*, 2007; *Balikhin et al.*, 2011; *Wing et al.*, 2016).  
72 However,  $V_{sw}$  negatively correlates with  $n_{sw}$  (e.g., *Wing et al.*, 2016; *Borovsky*, 2020). This raises  
73 the question that given the  $V_{sw}-n_{sw}$  negative correlation, if  $V_{sw}$  positively correlates with radiation  
74 belt electron  $J_e$ , then the negative correlation of  $n_{sw}$  with radiation belt electron  $J_e$  may simply be  
75 coincidental. Conversely, given the solar wind property, if  $n_{sw}$  negatively correlates with  $J_e$ , then  
76 the positive correlation of  $V_{sw}$  and radiation belt  $J_e$  may simply be coincidental. Of course,  $n_{sw}$  and

77  $V_{sw}$  may independently exert influence on the radiation belt electrons. In that case, how can one  
78 isolate the effect of an individual solar wind parameter?

79         A few studies attempted to separate the effects of  $n_{sw}$  from  $V_{sw}$  by using methods that bin  
80 the data into small intervals of  $V_{sw}$  and  $n_{sw}$  or explicitly select events when one parameter is nearly  
81 constant while the effect of the other parameter is investigated (e.g., *Lyatsky and Khazanov, 2008*).  
82 This type of analysis has offered insights into the solar wind driving of the radiation belt  $J_e$ .  
83 However, holding one parameter nearly constant, either explicitly or through small binning, in  
84 order to investigate the second parameter does not completely eliminate the effect of the first  
85 parameter. For example, selecting events when  $V_{sw}$  is nearly constant to investigate the effect of  
86  $n_{sw}$  does not completely eliminate the effect of  $V_{sw}$  because  $V_{sw}$  or its effect is not zero. Nearly  
87 constant but high  $V_{sw}$  can still affect the correlation of  $n_{sw}$  and radiation belt  $J_e$ . Moreover, it does  
88 not address the question of how much additional information  $n_{sw}$  provides to  $J_e$ , given  $V_{sw}$  and vice  
89 versa. Many studies have shown that other solar wind parameters and magnetospheric parameters  
90 can also contribute to  $J_e$  variations [e.g., *Balikhin et al., 2011; Rigler et al., 2007; Vassiliadis et*  
91 *al., 2005; Li et al., 2005; Simms et al., 2014;*], but presently, it is not entirely clear quantitatively  
92 given a main driver, e.g.,  $V_{sw}$  (or  $n_{sw}$ ), how much additional information these parameters provide  
93 to  $J_e$ .

94         The solar wind–magnetospheric system has been shown to be nonlinear [e.g., *Wing et al.,*  
95 *2005; Johnson and Wing, 2005; Reeves et al., 2011; Kellerman and Shprits, 2012; Wing et al.,*  
96 *2016*]. For nonlinear system, linear correlational analysis can be misleading [e.g., *Balikhin et al.,*  
97 *2010; 2011*].

98         Information theory has been shown to be quite useful for studies of the Earth’s  
99 magnetosphere (*Balasis et al., 2009; Stumpo et al., 2020; March et al., 2005; Johnson and Wing,*

100 2005; 2014, *Wing et al.*, 2016; *Johnson et al.*, 2018; *Runge et al.*, 2018; *Papadimitriou et al.*, 2020;  
101 *Manshour et al.*, 2021), Kronian magnetosphere (*Wing et al.*, 2020), and the Sun (*Consolini et al.*,  
102 2009; *Wing et al.*, 2018; *Snelling et al.*, 2020). Information theory can help identify nonlinearities  
103 in the system and information transfer from one variable to another. Moreover, information theory  
104 can also help untangle the drivers that are positively or negatively correlated with one another  
105 (*Wing et al.*, 2016; *Wing and Johnson*, 2019).

106 *Wing et al.* (2016) used information theoretic tools to study the solar wind driving of the  
107 radiation belt electrons. The study used the publicly available Los Alamos National Laboratory  
108 (LANL) satellite data, which provide geosynchronous electron flux measurements at daily  
109 resolution. When the study began in early 2015, the Radiation Belt Storm Probes (RBSP) or Van  
110 Allen Probes satellites had only been operational for a few years, and there was not enough data  
111 for a statistical study. Usage of the daily resolution of the radiation belt electron data prevented  
112 *Wing et al.* (2016) from resolving any electron response lag time to the solar wind drivers that is  
113 shorter than 24 hours. For example, the LANL MeV electron  $J_e$  negatively correlates with daily  
114 averaged  $n_{sw}$  with a lag time ( $\tau$ ) of 1 day. *Zhao et al.* (2017) correlated daily averaged radiation  
115 belt electron phase space density (PSD) with  $n_{sw}$  and also obtained  $\tau = 1$  day for MeV electrons ( $\mu$   
116  $> 700$  MeV  $G^{-1}$ ). However, if the effect of  $V_{sw}$  is properly removed,  $\tau$  shifts to 0 day (*Wing et al.*,  
117 2016). In other words, the radiation belt electron response to  $n_{sw}$  is less than 24 hr. However, the  
118 study could not pinpoint exactly how much less than 24 hr with the daily resolution LANL data.  
119 Another limitation of *Wing et al.* (2016) study is that the LANL data only provide the electron  
120 observations at a fixed radial distance from the Earth, at the geosynchronous orbit.

121 Since *Wing et al.* (2016) study, RBSP has gathered seven years of radiation belt electron  
122 data (2013-2019) at high time resolution ( $< 1$  min) from  $2 < L^* < 7$ . Hence, the time is ripe for a

123 follow up study that uses the RBSP data. As in *Wing et al. (2016)*, the present study uses  
124 information theory to determine the solar wind and magnetospheric drivers of the radiation belt  
125 electrons and the response time scales. In order to focus on the drivers of the nonadiabatic heating  
126 and acceleration, the present study examines the response of the radiation belt electron phase space  
127 density (PSD) to the drivers.

128

## 129 **2. Data set**

130 Van Allen Probe (or RBSP) mission, which was launched in 2012, had two identically  
131 instrumented spacecraft in near-equatorial orbit (about  $10^\circ$  inclination) with perigee at 600 km  
132 altitude and apogee at  $5.8 R_E$  geocentric (*Mauk et al., 2013*). The MAGnetic Electron Ion  
133 Spectrometer (MagEIS) and Relativistic Electron-Proton Telescope (REPT) instruments are part  
134 of the Energetic particle, Composition, and Thermal plasma Suite (ECT) instrument on board of  
135 RBSP (*Spence et al., 2013*). MagEIS measured the energy range of 30 keV to 4 MeV for electrons  
136 and 20 keV to 1 MeV for ions (*Blake et al., 2013*) while REPT measured electrons with energy  
137 range 1.5 to  $\geq 10$  MeV and protons with energy range 20 to 75 MeV (*Baker et al., 2012*).

138 The present study focuses only on the electron data. Radiation belt electron dynamics can  
139 often be described by their adiabatic invariants and PSD ( $\mu$ , K,  $L^*$ ) where  $\mu$  = the first adiabatic  
140 invariant related to the gyromotion perpendicular to the magnetic field line, K = the second  
141 adiabatic invariant related to the bounce motion along the field line, and L or  $L^*$  = the third  
142 adiabatic invariant related to the curvature and gradient drift motion around the Earth (actually  $L^*$   
143 is inversely proportional to the third invariant  $\Phi$ ) (*Roederer, 1970; Schulz and Lanzerotti, 1974;*  
144 *Lejosne and Kollman, 2020*).

145 Data from the RBSP-ECT Combined dataset (*Boyd et al., 2021*) are used to obtain electron

146 PSD as a function of adiabatic invariants across the full MagEIS and REPT energy range. The  
 147 PSD is calculated using the techniques outlined in (Turner *et al.*, 2014a; 2014b; Boyd *et al.*, 2014)  
 148 at  $\sim 5$  min time cadence. The PSD calculation uses TS04 magnetic field model (Tsyganenko and  
 149 Sitnov, 2005). We select the electrons with  $\mu = 725\text{--}875$  MeV G<sup>-1</sup> and  $K = 0.09\text{--}0.13 R_E$  G<sup>-0.5</sup>.  
 150 These electrons have an average energy of  $\sim 1.6$  MeV, but they range from 480 keV to 4.8 MeV  
 151 spanning over L\* of 2.5 to 6.8.

152 The solar wind, AL, and SYM-H data 2013-2019 come from OMNI 1 min resolution data  
 153 provided by NASA (<http://omniweb.gsfc.nasa.gov/>). Both the PSD and OMNI data 2013-2019  
 154 are averaged with 30 min sliding window.

155 We merge each OMNI solar wind parameter ( $V_{sw}$ ,  $n_{sw}$  etc.) with the RBSP electron PSD.  
 156 As described in Section 3, we perform time shifted correlation and conditional mutual information  
 157 analysis to determine the radiation belt electron response lag time up to 120 hr. Depending on the  
 158 solar wind parameter, typically the merged datasets have approximately 60,000 to 85,000 points.  
 159

### 160 3. Methodology

161 Mutual information and conditional mutual information are briefly described below, but  
 162 they are also described in Balasis *et al.* (2013), and Wing *et al.* (2016, 2018).

163 Let variables  $x$  and  $y$  have  $n$  and  $m$  elements in sets  $\aleph_1$  and  $\aleph_2$ , respectively,

$$164 \quad x \in \{\hat{x}_1, \hat{x}_2, \dots, \hat{x}_n\} \equiv \aleph_1; \quad y \in \{\hat{y}_1, \hat{y}_2, \dots, \hat{y}_m\} \equiv \aleph_2 \quad (1)$$

165 The entropy associated with each of the variables is defined as

$$166 \quad H(x) = - \sum_{\aleph_1} p(\hat{x}) \log p(\hat{x}); \quad H(y) = - \sum_{\aleph_2} p(\hat{y}) \log p(\hat{y}) \quad (2)$$

167 where  $p(\hat{x})$  is the probability of finding the word  $\hat{x}$  in the set of  $x$ -data and  $p(\hat{y})$  is the probability  
 168 of finding word  $\hat{y}$  in the set of  $y$ -data. To examine the relationship between the variables, we

169 extract the word combinations  $(\hat{x}, \hat{y})$  from the dataset. The joint entropy is defined by

$$170 \quad H(x, y) = - \sum_{\mathfrak{N}_1 \mathfrak{N}_2} p(\hat{x}, \hat{y}) \log p(\hat{x}, \hat{y}) \quad (3)$$

171 where  $p(\hat{x}, \hat{y})$  is the probability of finding the word combination  $(\hat{x}, \hat{y})$  in the set of  $(x, y)$  data.

172 Then, the mutual information (MI) (Tsonis, 2001; Li, 1990; Darbellay and Vajda, 1999) is defined  
173 as

$$174 \quad \text{MI}(x, y) = H(x) + H(y) - H(x, y) \quad (4)$$

175 MI compares the uncertainty of measuring variables jointly with the uncertainty of  
176 measuring the two variables independently. MI gives a measure of linear and nonlinear  
177 dependence between two variables. Conditional mutual information (CMI) gives a measure of  
178 conditional dependency with respect to a conditioner variable  $z$  where  $\hat{z} \in \{z_1, z_2, \dots, z_k\} \equiv \mathfrak{N}_3$ .

179 CMI is defined as (Wyner, 1978)

$$180 \quad \text{CMI}(x, y | z) = \sum_{\mathfrak{N}_1 \mathfrak{N}_2 \mathfrak{N}_3} p(\hat{x}, \hat{y}, \hat{z}) \log \frac{p(\hat{x}, \hat{y} | \hat{z})}{p(\hat{x} | \hat{z}) p(\hat{y} | \hat{z})} = H(x, z) + H(y, z) - H(x, y, z) - H(z) \quad (5)$$

181 CMI determines the mutual information between  $x$  and  $y$  given that  $z$  is known. In other  
182 words, CMI determines how much additional information is known given another variable. If  $x$  or  
183  $y$  is known based on  $z$ , then  $\text{CMI}(x, y | z) = 0$ . The maximum CMI occurs when  $x$  and  $y$  do not  
184 depend on the conditioner variable  $z$ , in which case  $\text{CMI}(x, y | z) = \text{MI}(x, y)$  and the maximum CMI  
185 and MI is  $\max(H(x), H(y))$ . CMI is a special case of the more general conditional redundancy that  
186 allows the variable  $z$  to be a vector (e.g., Prichard and Theiler, 1995; Johnson and Wing, 2014).

187 Herein, we use the short hand Pearson's linear correlation  $\text{corr}(x(t), y(t + \tau))$  as  $\text{corr}(x \rightarrow$   
188  $y)$ . Likewise,  $\text{CMI}(x(t), y(t + \tau) | z(t))$  is denoted as  $\text{CMI}(x \rightarrow y | z)$ . We define  $i_{tr}$  = information  
189 transfer =  $\text{CMI}(x \rightarrow y | z) - \text{mean noise}$ , where  $\text{noise} = \text{CMI}(\text{sur}(x) \rightarrow y | z)$ ,  $\text{sur}(x)$  is the surrogate  
190 data of  $x$  and is obtained by randomly permuting the order of the time series of array  $x$ . Mean and  
191  $\sigma$  of the noise are calculated from an ensemble of 100 values of  $\text{CMI}(\text{sur}(x) \rightarrow y | z)$ . The mean

192 noise and  $\sigma$  estimate are valuable diagnostics included on all of the CMI data presented here: any  
193 CMI outside the  $3\sigma$  noise range are significant and CMI less than the  $3\sigma$  from the noise is  
194 considered not significant. Furthermore, we define  $i_{tr\_max} = i_{tr}$  at the peak  $\tau$  and significance =  
195  $i_{tr}/\sigma$ .

196 We note that the surrogate data is constructed to be consistent with our null hypothesis. In  
197 our correlation and CMI analysis, the null hypothesis is that variables  $x$  and  $y$  are unrelated  
198 (random). We test whether  $x$  and  $y$  are (linearly and nonlinearly) correlated. If we would like to  
199 determine the degree to which  $x$  and  $y$  are nonlinearly correlated or if we would like to remove the  
200 linear correlation from our CMI, then we could use a red noise type surrogate such that CMI would  
201 be insignificant if  $x$  and  $y$  are linearly correlated. We could also use the method described in  
202 *Prichard and Theiler (1995)* and later used in *Johnson and Wing (2005)* to construct surrogates  
203 that share the same linear correlations as the original data to isolate the nonlinear dependence. As  
204 a future study, it would be interesting to explore different types of surrogate data.

205

## 206 **4. Applying information theory to radiation belt MeV electron data**

### 207 **4.1 A simple example of an application of conditional mutual information (CMI)**

208 CMI can be quite useful to untangle the effects of multiple drivers of a system. Figure 1  
209 presents a simple example that illustrates this point. Figure 1a plots  $\text{corr}(V_{sw} \rightarrow \text{PSD})$ . The figure  
210 shows that  $V_{sw}$  positively correlates with PSD and the correlation peaks at  $\tau = 38$  hr. The  
211 correlation is significant with  $n = 84,729$  points and correlation coefficient ( $r$ ) = 0.47 and  $p < 0.01$ .  
212 Previous studies have also found good correlations between  $V_{sw}$  and radiation belt electrons with  
213  $\sim 2$  days lag and the lag time has been attributed to the time scale to accelerate the electrons to 1–  
214 2 MeV due to local acceleration, radial transport, or some other acceleration mechanisms (e.g.,

215 *Baker et al.*, 1990; *Shprits et al.*, 2008; *Reeves et al.*, 2011; *Li et al.*, 2005; *Ukhorskiy et al.*, 2005;  
216 *Summers et al.*, 2007; *Thorne et al.*, 2013; *Turner and Li*, 2008; *Boyd et al.*, 2018). Figure 1b plots  
217 the  $\text{corr}(n_{sw} \rightarrow \text{PSD})$ , which shows that  $n_{sw}$  negatively correlates with PSD with a minimum at  $\tau =$   
218 15 hr,  $r = -0.22$ ,  $n = 84,729$ ,  $p < 0.01$ . *Lyatsky and Khazanov* (2008) also found the same negative  
219 correlation at  $\tau = 15$  hr. The negative correlation has been previously attributed to the  
220 magnetopause shadowing: an increase in  $n_{sw}$  would increase solar wind dynamic pressure ( $P_{dyn}$ ),  
221 which would compress the magnetosphere leading to radiation belt electron losses (e.g., *Li et al.*,  
222 2001; *Kellerman and Shprits*, 2012; *Turner et al.*, 2012; *Ukhorskiy et al.*, 2006). Figure 1c plots  
223 the  $\text{corr}(P_{dyn} \rightarrow \text{PSD})$ , which shows that the radiation belt electron response to  $P_{dyn}$ , which is  $\sim n_{sw}$   
224  $V_{sw}^2$ , has dual modes. At small  $\tau$ ,  $\tau < \sim 20$  hr,  $P_{dyn}$  negatively correlates with PSD, which is similar  
225 to the effect of  $n_{sw}$  and can be attributed to the magnetopause shadowing. However, at large  $\tau$ ,  $\tau$   
226  $> 40$  hr,  $P_{dyn}$  positively correlates with PSD, which is similar to the effect of  $V_{sw}$ . The correlations  
227 are significant at  $p < 0.01$  and  $n = 82,652$ . *Zhao et al.* (2017) correlated  $P_{dyn}$  with PSD at daily  
228 time resolution and also found a dual response mode of the PSD to  $P_{dyn}$ . Figure 1d plots  $\text{CMI}(P_{dyn}$   
229  $\rightarrow \text{PSD} | n_{sw})$ , which shows the dependence of PSD on  $P_{dyn}$ , given  $n_{sw}$ . It shows that if we remove  
230 the effect of  $n_{sw}$ , the effect of  $P_{dyn}$  on PSD is similar to that of  $V_{sw}$  in Figure 1a, as expected. The  
231 CMI curve does not match exactly the correlation curve in Figure 1a because the CMI curve takes  
232 into account the nonlinearities in the data.

233 In Figure 1d, the green solid and dashed curves are mean noise and  $3\sigma$  from the noise,  
234 respectively. The significance at peak  $\tau = 51$  hr is  $203\sigma$  and hence it is significant.

235

## 236 4.2 Isolating the effects of the solar wind velocity from density and vice versa

237 *Wing et al.* (2016) isolated the effects of  $V_{sw}$  and  $n_{sw}$  on the radiation belt electron  $J_e$  using

238 CMI. They found that  $\text{CMI}(V_{sw} \rightarrow J_e | n_{sw})$  peaks at  $\tau = 2-3$  days while  $\text{CMI}(n_{sw} \rightarrow J_e | V_{sw})$  peaks  
239 at  $\tau = 0$  day. However, the lag times,  $\tau$ , in *Wing et al. (2016)* are imprecise due to the usage of the  
240 daily resolution LANL electron data. Furthermore, LANL data are limited to GEO, but the outer  
241 belt is not accurately represented by data at GEO alone, especially for the heart of the outer belt  
242 between  $4 \leq L \leq 5$  (e.g., *Baker et al., 2019b*). In the present study, we recompute the CMIs using  
243 30 min resolution RBSP PSDs representative of  $\sim 1$  MeV electrons throughout the entire outer belt  
244 and solar wind data. Furthermore, by using electron PSD for fixed values of the first and second  
245 adiabatic invariants in place of  $J_e$  as a function of energy, the data used here further deconvolute  
246 the energy and pitch angle dependencies of the underlying physical processes that drive radiation  
247 belt enhancements and losses.

248 Figures 2a and 2b replot  $\text{corr}(V_{sw} \rightarrow \text{PSD})$  and  $\text{corr}(n_{sw} \rightarrow \text{PSD})$ , which are plotted in  
249 Figures 1a and 1b, respectively. However,  $V_{sw}$  negatively correlates with  $n_{sw}$  and  $\text{corr}(V_{sw} \rightarrow n_{sw})$   
250 has a minimum at  $\tau = 15$  hr ( $r = -0.48$ ,  $n = 105,459$ ,  $p < 0.01$ ), as shown in Figure 2c. For  
251 completeness, Figure 2c also plots  $\text{corr}(n_{sw} \rightarrow V_{sw})$  (red curve), which has  $r = 0.10$ ,  $p < 0.01$ . The  
252 figure shows that  $|\text{corr}(V_{sw} \rightarrow n_{sw})| > |\text{corr}(n_{sw} \rightarrow V_{sw})|$ . The negative correlation between  $V_{sw}$  and  
253  $n_{sw}$  have been previously reported with similar  $\tau$  (e.g., *Wing et al., 2016; Maggiolo et al., 2017;*  
254 *Borovsky, 2020*). Note that  $\tau$  may vary from year to year (*Wing et al., 2016*), leading to an overall  
255 broadening of the peak when considering an ensemble of intervals across the solar cycle.

256 Given that  $V_{sw}$  negatively correlates with  $n_{sw}$ , if  $n_{sw}$  negatively correlates with PSD (Figure  
257 2b), then the positive correlation between  $V_{sw}$  and PSD may be deemed just coincidental. Figure  
258 2d, which plots  $\text{CMI}(V_{sw} \rightarrow \text{PSD} | n_{sw})$ , shows that even after the effect of  $n_{sw}$  has been removed,  
259 there is still strong information transfer from  $V_{sw}$  to PSD, which peaks at  $\tau = 46$  hr ( $n = 78,811$ ,  
260 significance =  $378\sigma$ ). Apparently, removing the effect of  $n_{sw}$ , shifts the peak to the right. The lag

261 time of  $\tau = 46$  hr obtained from CMI is considered a more accurate radiation belt electron response  
262 time to the  $V_{sw}$  (the time scale for electron acceleration to 1-2 MeV energy range) than the lag time  
263 of  $\tau = 38$  hr obtained from Pearson's correlation.

264 We can also check whether or not  $\text{corr}(n_{sw} \rightarrow \text{PSD})$  is coincidental. Figure 2e plots  
265  $\text{CMI}(n_{sw} \rightarrow \text{PSD} | V_{sw})$ , which shows two peaks. The primary peak at  $\tau = 7-11$  hr ( $n = 78,811$ ,  
266 significance =  $52\sigma$ ) can be compared to the minimum in  $\text{corr}(n_{sw} \rightarrow \text{PSD})$  in Figure 2b.  
267 Apparently, removing the effect of  $V_{sw}$ , shifts the peak to the left. The lag time of  $\tau = 7-11$  hr is  
268 considered a more accurate radiation belt electron response time to the magnetopause shadowing  
269 than the  $\tau = 15$  hr obtained from the correlational analysis. Note that CMI only gives positive  
270 values and does not distinguish negative from positive correlations. As such, CMI is analogous to  
271  $|r|$ .

272 Figure 2e shows that there is a secondary broad peak at  $\tau = 80-120$  hr (or even larger).  
273 Unlike the primary peak, which is a negative correlation, the secondary peak is a positive  
274 correlation with  $n_{sw}$ . In order to show this, we plot  $\text{PSD}(t + \tau)$  vs.  $V_{sw}(t)$  vs.  $n_{sw}(t)$  for  $\tau = 0, 5, 10,$   
275  $40, 80, 100,$  and  $120$  hr in Figure 3 panels a to g, respectively. In all panels, it can be seen that at  
276 high  $V_{sw}$ ,  $V_{sw} > \sim 500$  km s<sup>-1</sup>,  $V_{sw}$  positively correlates with the radiation belt electron PSD as  
277 previously reported (Reeves *et al.*, 2011; Wing *et al.*, 2016). However, for  $V_{sw} < \sim 450$  km s<sup>-1</sup>, and  
278 small  $\tau$  ( $\tau = 0, 5,$  and  $10$  hr),  $n_{sw}$  negatively correlates with the radiation belt electron PSD, e.g.,  
279 yellow and brown region clustering at the bottom, which corresponds to the first and primary peak  
280 in Figure 2e. At  $\tau = 40$  hr, there is little or no correlation between  $n_{sw}$  and the PSD, which  
281 corresponds to the minimum in Figure 2e. However, at large  $\tau$ ,  $\tau = 80, 100, 120$  hr and  $V_{sw} < \sim 450$   
282 km s<sup>-1</sup>,  $n_{sw}$  positively correlates with PSD, e.g., yellow and brown region clustering at the top,  
283 which corresponds to the secondary peak in Figure 2e. This positive correlation between  $n_{sw}$  and

284 electron PSD at large  $\tau$  cannot be seen in the  $\text{corr}(n_{sw} \rightarrow \text{PSD})$  in Figure 2b because the effect has  
285 been smeared or cancelled out by the effects for all  $V_{sw}$  where high electron PSD can correspond  
286 to high and low  $n_{sw}$  (Figure 3 panels e–g).

287 It is not clear what causes the positive linear and nonlinear correlation between  $n_{sw}$  and  
288 electron PSD at large  $\tau$ .  $n_{sw}$  may be a proxy for another parameter. For example,  $n_{sw}$  positively  
289 correlates with |IMF B| (Borovsky, 2020; Maggiolo et al., 2017). Whatever the mechanism is, our  
290 result shows that the time scale for such process to energize electrons to 1–2 MeV is slow,  $> 80$   
291 hr.

292

### 293 **4.3 The radial dependence of the radiation belt electrons on the solar wind density and** 294 **velocity**

295 The effects of the  $n_{sw}$  and  $V_{sw}$  on the radiation belt electrons have a dependence on the  
296 radial distance or  $L^*$  (e.g., Baker et al., 2019a; Tang et al., 2017; Turner et al., 2019; Zhao et al.,  
297 2017; W. Li et al., 2014). In order to show this, PSD data are binned from  $L^* = 3$  to 6.5 into 7 bins  
298 with bin width = 0.5. The data coverage for the electrons with  $\mu = 725\text{--}875 \text{ MeV G}^{-1}$  and  $K =$   
299  $0.09\text{--}0.13 R_E \text{ G}^{-0.5}$  is poor for  $L^* < 3$  and  $L^* > 6.5$ . Figure 4 shows  $\text{corr}(n_{sw} \rightarrow \text{PSD})$  as a function  
300 of  $L^*$ . It shows that the correlation is near 0 at  $L^* = 3\text{--}3.5$ , but slowly decreases with increasing  
301  $L^*$ . Except for  $L^* = 3\text{--}3.5$  ( $n = 8435$ , Figure 4a), the correlations are significant ( $p < 0.01$ ) at the  
302 minimum  $\tau$  ( $\tau = 15, 16, 17, 17, 17, 13 \text{ hr}$ ),  $r = (-0.086, -0.17, -0.27, -0.31, -0.34, -0.50)$ , ( $n =$   
303  $8,302, 11,481, 17,7891, 27,060, 6,236, 528$ ) for panels (b–g), respectively. The number of points  
304 in  $L^* = 6\text{--}6.5$  (Figure 4g) is the fewest, which results in a noisier correlation. However, as  
305 discussed in the Sections 1, 4.1, and 4.2, the correlation may be inaccurate because  $n_{sw}$  negatively  
306 correlates with  $V_{sw}$  (Figure 2c) and the system is nonlinear (Wing et al., 2016). Hence, we calculate

307 CMI( $n_{sw} \rightarrow \text{PSD} | V_{sw}$ ) for the PSD data in the same bins. The results are plotted in Figure 5. The  
 308 figure shows that the effect of  $n_{sw}$  on PSD is at the noise level at  $L^* = 3-4.5$ , is significant at  $L^* =$   
 309  $5-6$ , and back to the noise level at  $L^* = 6-6.5$ . However, the result for  $L^* = 6-6.5$  is considered  
 310 not reliable because of the small number of points ( $n = 528$ ). The response lag times based on the  
 311 first peak are  $\tau = 9, 10, \text{ and } 7 \text{ hr}$  ( $n = 16,629, 25,238, \text{ and } 5865$ ; significance = 17, 42, and 5  $\sigma$ ) at  
 312  $L^* = 4.5-5, 5-5.5, \text{ and } 5.5-6$ , respectively. Notice that the response lag times are quite different  
 313 in Figures 4 and 5.

314 For completeness, we examine the effect of  $P_{dyn}$  on the PSD. Figure 6 plots CMI( $P_{dyn} \rightarrow$   
 315  $\text{PSD} | V_{sw}$ ) as a function of  $L^*$  in the same format as Figure 5. It shows that the effect of  $P_{dyn}$  on  
 316 PSD is similar to that of  $n_{sw}$ , as expected. The largest effect of  $P_{dyn}$  on electron PSD can be found  
 317 at  $L^* = 4.5-6$ . (significance = 32, 53, 17  $\sigma$  for  $L^* = 4.5-5, 5-5.5, \text{ and } 5.5-6$ ), respectively. The  
 318 number of points in each bin in Figure 5 is the same as that in Figure 6. Taken together, Figures  
 319 5 and 6 suggest that the magnetopause shadowing is effective only at  $L^* = 4.5-6$ . At  $L^* = 6-6.5$ ,  
 320 there is a high variability of PSD and the bin has fewest number of points and hence the result is  
 321 inconclusive.

322 Moreover, the significances are higher for the first peak in Figure 6 panels d-f than their  
 323 counterparts for CMI( $n_{sw} \rightarrow \text{PSD} | V_{sw}$ ) in Figure 5 panels d-f, suggesting that the real causal  
 324 parameter for the magnetopause shadowing is  $P_{dyn}$  rather than  $n_{sw}$ . However, the opposite is true  
 325 for the secondary peak. This would suggest that the secondary peak may be more causally related  
 326 to  $n_{sw}$  (or its proxy) than  $P_{dyn}$ .

327 We perform the same analysis with  $V_{sw}$  and electron PSD. Figure 7 shows  $\text{corr}(V_{sw} \rightarrow$   
 328  $\text{PSD})$  as a function of  $L^*$  in the same format as Figure 4. The correlations are all significant at  $p <$   
 329  $0.01$  at the maximum  $\tau$  ( $\tau = 40-120, 30-120, 38, 30, 37, 45, 30-90 \text{ hr}$ ), ( $r = 0.14, 0.27, 0.42, 0.57,$

330 0.62, 0.64, 0.70) for  $L^* = 3-3.5, 3.5-4, 4-4.5, 4.5-5, 5-5.5, 5.5-6,$  and  $6-6.5,$  respectively. Baker  
 331 et al. (2019a) also found higher correlation with increasing  $L$  ( $r = 0.32, 0.51,$  and  $0.61$  for  $L = 3.5,$   
 332  $4.5,$  and  $5.5,$  respectively). For comparison, Figure 8 plots  $\text{CMI}(V_{sw} \rightarrow \text{PSD} | n_{sw})$  as a function of  
 333  $L^*$  in the same format as Figure 5. The number of points in each bin is the same as that in Figure  
 334 5. Figure 8 shows that the CMI is at the noise level at  $L^* = 3-3.5$  (panel a), unlike its counterpart  
 335 in Figure 7a. At  $L^* = 3.5-4.5,$  the CMI has a broad peak from  $\tau \sim 50-100$  hr (or larger for the case  
 336  $L^* = 3.5-4$ ) and the peaks are significant (peak significance = 18 and 46  $\sigma$  for  $L^* = 3.5-4$  and 4-  
 337 4.5), respectively. At  $L^* = 4.5-6,$  the CMI peaks are narrower (peak  $\tau = 40, 46, 57$  hr; significance  
 338 = 236, 399, and 100  $\sigma$ ), respectively. Interestingly, at  $\tau = 6-6.5,$  the peak broadens again but  
 339 remains significant (peak significance = 19  $\sigma$ ). To help visualize the evolution of the CMI, red  
 340 dashed vertical lines at  $\tau = 40$  hr is drawn in Figure 8.

341 The radiation belt electron response lag times as a function of  $L^*$  is further examined in  
 342 Figure 9. The figure shows the normalized  $i_{lr}$  for each  $L^*$  bin (the blue curve subtracted by the  
 343 solid green curve in Figure 8). The orange and yellow color correspond roughly to the top 20% of  
 344  $i_{lr}$  in each  $L^*$  bin. At  $L^* = 4.5-5.5,$  response lag time peaks around  $\tau = 35-50$  hours, which is  
 345 consistent or close to the previously reported time scale of 2 days to accelerate electrons to 1-2  
 346 MeV (Paulikas and Blake, 1979; Reeves et al., 2011; Li et al., 2001; Wing et al., 2016). At higher  
 347  $L^*, L^* = 5.5-6,$  the peak broadens and shifts to larger  $\tau, \tau = 45-65$  hr. At  $L^* = 6-6.5,$  the peak is  
 348 even broader at  $\tau = 40-100$  hr. At lower  $L^*, L^* = 4-4.5$  and  $3.5-4,$  one can also see successive  
 349 broadening of the peak as the peak shifts to larger  $\tau, \tau = 35-55$  hr and  $\tau = 45-60$  hr, respectively.  
 350 Section 5.3 discusses how the result is consistent with local acceleration where the peak of the  
 351 electron acceleration region is located at  $L^* = 4.5-5.5,$  from where electrons diffuse outward and  
 352 inward.

353

#### 354 4.4 The dependence of the radiation belt electrons on the magnetospheric state

355 The radiation belt electrons depend not just on the external (solar wind) drivers but also  
356 the internal state of the magnetosphere (e.g., *Baker et al.*, 2019a; *Borovsky and Denton*, 2014;  
357 *Borovsky*, 2017; *Zhao et al.*, 2017). In order to determine how the radiation belt electrons depend  
358 on the internal state of the magnetosphere, we examine the relationships of the electron PSD with  
359 AL and SYM-H indices. SYM-H index gives a measure of the strength of the ring current and  
360 storm (*Iyemori*, 1990) while AL gives a measure of the strength of the westward auroral electrojets  
361 and substorm (*Davis and Sugiura*, 1966). SYM-H is similar to Disturbance Storm Time ( $D_{st}$ )  
362 index (*Dessler and Parker*, 1959), except that SYM-H index is defined to have a one minute time  
363 resolution whereas  $D_{st}$  index has one hour resolution. Both SYM-H (proxy for storms) and AL  
364 (proxy for substorms) can be associated with plasma injections to the inner magnetosphere, which  
365 can enhance the whistler mode chorus waves and provide the seed population for the local  
366 acceleration (*Katus et al.*, 2013; *Wing et al.*, 2014).

367 Figure 10a plots  $\text{corr}(\text{AL} \rightarrow \text{PSD})$ , which shows that AL negatively correlates with electron  
368 PSD with a minimum  $\tau \sim 53$  hr ( $n = 70,125$ ,  $r = -0.33$ ,  $p < 0.01$ ). A smaller (more negative) AL  
369 corresponds to a more intense substorm and larger auroral electrojets. Figure 10b plots  $\text{corr}(V_{sw}$   
370  $\rightarrow \text{PSD})$  (same as Figure 1a). Figure 10c plots  $\text{corr}(V_{sw} \rightarrow \text{AL})$ , which shows that the auroral  
371 electrojet response to  $V_{sw}$  is fairly quick  $\tau = 0$  hr ( $< 30$  min) ( $n = 82,995$ ,  $r = -0.40$ ,  $p < 0.01$ ).  
372 Similar correlation was obtained by *Smirnov et al.* (2020). Given the positive correlation of  $V_{sw}$   
373 and electron PSD, and the negative correlation of  $V_{sw}$  and AL, one may ask the question whether  
374 the negative correlation between AL and electron PSD may just simply be coincidental or whether  
375 AL can independently affect PSD. Figure 10d plots  $\text{CMI}(\text{AL} \rightarrow \text{PSD} | V_{sw})$ , which shows that the

376 radiation belt electrons still have strong dependence on AL even after the effect of  $V_{sw}$  has been  
 377 removed. The CMI peaks at  $\tau \sim 50\text{--}80$  hr (significance =  $58\sigma$ ,  $n = 64,564$ ), suggesting that perhaps  
 378 the time scale to accelerate electrons to 1–2 MeV energy range from the time of substorm onset or  
 379 substorm particle injection is about 50–80 hr. This time scale is an ensemble average for all  $L^*$ .  
 380 To help visualize the comparison of Figures 10a and 10d, a dashed vertical red line is drawn at  $\tau$   
 381 = 53 hr (the minimum of  $\text{corr}(\text{AL} \rightarrow \text{PSD})$ ). It shows that removing the effect of  $V_{sw}$ , shifts the  
 382 peak to the right (to a larger  $\tau$ ) by a little bit ( $\sim 10$  hr).

383 Figure 11 displays the normalized  $i_{tr}$  as a function of  $L^*$  and  $\tau$  where  $i_{tr} = \text{CMI}(\text{AL} \rightarrow \text{PSD} |$   
 384  $V_{sw}) - \text{mean noise}$  in the same format as Figure 9. The  $i_{tr}$  is at the noise level at  $L^* = 3\text{--}3.5$  ( $n =$   
 385  $6409$ ). At  $L^* = 6\text{--}6.5$ , there is a high variability in PSD and the bin has the fewest number of  
 386 points ( $n = 216$ ) and hence the result is unclear and not shown. The region with the largest  
 387 significance is  $L^* = 4.5\text{--}5$  and  $5\text{--}5.5$  with peak  $\tau = 40\text{--}80$  and  $45\text{--}85$  hr and peak significance =  
 388  $33$  and  $38 \sigma$  ( $n = 13,825$  and  $20,527$ ) respectively. The peak shifts to larger  $\tau$ ,  $\tau = 75\text{--}100$  hr, at  
 389  $L^* = 5.5\text{--}6$  ( $n = 4686$ , peak significance =  $18\sigma$ ). At  $L^* = 4\text{--}4.5$ , the peak is broad,  $\tau = 35\text{--}80$  hr  
 390 ( $n = 8802$ ; peak significance =  $19 \sigma$ ). At  $L^* = 3.5\text{--}4$ , the peak is broad at  $\tau = 60\text{--}110$  hr, but the  
 391 peak significance is relatively small ( $n = 6379$ , peak significance =  $9 \sigma$ ). Section 5.3 discusses  
 392 this result in terms of local acceleration and subsequent inward and outward diffusion.

393 We perform similar analysis with SYM-H. Figure 12 is similar to Figure 10, except that it  
 394 is for SYM-H instead of AL index. Figure 12a plots  $\text{corr}(\text{SYM-H} \rightarrow \text{PSD})$ , which shows that  
 395 SYM-H negatively correlates with electron PSD with a minimum at  $\tau \sim 40$  hr ( $n = 91,589$ ,  $r = -$   
 396  $0.35$ ,  $p < 0.01$ ) while Figure 12b plots  $\text{corr}(V_{sw} \rightarrow \text{PSD})$  (same as Figure 10b).  $V_{sw}$  negatively  
 397 correlates with SYM-H and the correlation has a minimum at  $\tau = 2\text{--}4$  hr ( $n = 91,589$ ,  $r = -0.35$ ,  $p$   
 398  $< 0.01$ ) (Figure 12c), suggesting that the ring current response to  $V_{sw}$  has a lag time of about 2–4

399 hr. Similar correlation was obtained in previous studies (e.g., *Maggiolo et al.*, 2017). Figures 12  
400 a–c pose the same dilemma as Figures 10 a–c do for AL. That is, given the positive correlation of  
401  $V_{sw}$  and electron PSD and the negative correlation of  $V_{sw}$  and SYM-H, one may ask whether the  
402 negative correlation of SYM-H and PSD could just simply be coincidental or whether SYM-H  
403 provides additional information about PSD. Figure 12d plots  $\text{CMI}(\text{SYM-H} \rightarrow \text{PSD} | V_{sw})$ , which  
404 shows that SYM-H indeed provides additional information to electron PSD even after the effect  
405 of  $V_{sw}$  has been removed. The CMI peaks at  $\tau \sim 30\text{--}70$  hr ( $n = 84,729$ , significance =  $109 \sigma$ ),  
406 suggesting that perhaps the time scale to accelerate electrons to 1–2 MeV energy range from the  
407 time of ring current enhancement is about 30–70 hr. However, the effect of SYM-H has a  
408 dependence on radial distance, as discussed next.

409 Figure 13 plots  $i_{tr}$  as a function of  $L^*$  where  $i_{tr} = \text{CMI}(\text{SYM-H} \rightarrow \text{PSD} | V_{sw}) - \text{mean noise}$   
410 in the same format as Figure 11. At  $L^* = 6\text{--}6.5$ ,  $i_{tr}$  is at the noise level, which can be attributed to  
411 high PSD variabilities as well as small number of points ( $n = 336$ ). The highest peak significance  
412 can be found at  $L^* = 5 - 5.5$  (peak  $\tau = 20\text{--}55$  hr, significance =  $79\sigma$ ,  $n = 27,060$ ). The peak shifts  
413 to higher  $\tau$  at higher  $L^*$ . At  $L^* = 5.5\text{--}6$ , the peak can be found at  $\tau = 60\text{--}75$  hr ( $n = 6236$ , peak  
414 significance =  $26 \sigma$ ). At  $L^* = 4\text{--}4.5$  and  $4.5\text{--}5$ , the  $i_{tr}$  peaks at  $\tau = 30\text{--}60$  and  $30\text{--}75$  hr ( $n = 11,495$   
415 and  $17,924$ ; peak significance =  $38$  and  $47 \sigma$ , respectively). At  $L^* = 3.5\text{--}4$ , the peak is very broad  
416 at  $\tau = 20\text{--}120$  hr or even higher ( $n = 8317$ , peak significance =  $23 \sigma$ ). At  $L^* = 3\text{--}3.5$ , the CMI  
417 peaks at  $\tau = 110\text{--}120$  hr or even higher ( $n = 8435$ , peak significance =  $14$ ). Section 5.3 discusses  
418 this result in terms of local acceleration and the subsequent inward and outward diffusion.

419 It is worth noting that out of all the parameters that we have examined, only SYM-H can  
420 provide information about radiation belt electron PSD at  $L^* = 3\text{--}3.5$  albeit only a small amount.  
421 The CMI at  $L^* = 3\text{--}3.5$  and  $\tau < 100$  hr is low, which is consistent with *Turner et al.* (2019) study

422 that found storms have little effect on 1–2 MeV electrons at  $L < 3.5$  (see their Figure 2), but  
423 apparently at  $\tau > 100$  hr, the storm effect is significant but only moderately.

424

#### 425 **4.5 The rankings of solar wind and magnetospheric parameters by the information transfer** 426 **to the radiation belt electrons**

427 In the previous sections, we calculate the dependence of the PSD on  $V_{sw}$ ,  $n_{sw}$ ,  $P_{dyn}$ , AL, and  
428 SYM-H.  $V_{sw}$  transfers the most information to the PSD by significantly larger amount than any  
429 other solar wind variables. In this section, we calculate the CMI from other solar wind parameters  
430 to the PSD, given  $V_{sw}$ . Specifically, we calculate  $\text{CMI}(x \rightarrow \text{PSD} | V_{sw})$  where  $x = \text{IMF } |B|$ ,  $B_z < 0$ ,  
431  $B_z > 0$ ,  $B_y$ ,  $E_{sw}$ , and  $\sigma(\text{IMF } B)$ .

432 Table 1 ranks these parameters based on the information transfer to the radiation belt  
433 electron PSD, given  $V_{sw}$  for  $L^* = 3 - 6.5$ . The information transfer is calculated as  $i_{tr\_max} =$   
434 maximum of (CMI – mean noise). The information transfer from  $V_{sw}$  to the PSD is calculated  
435 from  $\text{CMI}(V_{sw} \rightarrow \text{PSD} | n_{sw})$ . It shows the dominance of  $V_{sw}$  in terms of information transfer to the  
436 PSD. SYM-H, which is ranked second, transfers only about a quarter as much information to the  
437 PSD. In Table 1, if the response lag time has a broad peak,  $\tau$  is reported as having a range of  
438 values. Table 1 shows that the radiation belt electron response lag time to the solar wind and  
439 magnetospheric parameters fall into two categories. The electron response with a small  $\tau$  ( $\tau < 15$   
440 hr) is a decrease in PSD (electron loss) while the response at large  $\tau$  ( $\tau > 40$  hr) is an enhancement  
441 in PSD.

442 Zhao et al. (2017) correlated PSD with solar wind ( $V_{sw}$ ,  $n_{sw}$ ,  $P_{dyn}$ ) and magnetospheric  
443 parameters (SYM-H, AL) and found that AL has the best correlation with PSD with  $t = 2\text{-}5$  days  
444 for  $\mu > 700$  MeV  $\text{G}^{-1}$ . However, their study differs from the present study in two key aspects: (1)

445 their study used daily resolution data; (2) more importantly, they did not remove the effect of  $V_{sw}$   
446 from AL, SYM-H, and other parameters. The second point is particularly consequential because  
447 AL negatively correlates with  $V_{sw}$  (Figure 10c) and some of the good correlation between AL and  
448 PSD can be partially attributed to the good correlation between  $V_{sw}$  and PSD.

449 Many of the parameters, namely IMF  $|B|$ , IMF  $B_z < 0$ , IMF  $B_y$ ,  $n_{sw}$ , and  $P_{dyn}$ , produce dual  
450 response modes in the radiation belt electrons. At small  $\tau$  ( $\tau < 15$  hr), the response is a decrease  
451 in PSD or electron loss while at large  $\tau$  ( $\tau > 30$  hr), the response is an enhancement in PSD. For  
452 these parameters, the ranking is based on the mode that has the higher  $i_{tr\_max}$ . The response to IMF  
453  $|B|$  has roughly the same  $i_{tr\_max}$  at small and large  $\tau$ , although Table 1 lists the response to the large  
454  $\tau$ . The response to IMF  $|B|$ , IMF  $B_z < 0$ , and IMF  $B_y$  at  $\tau < 15$  hr is electron loss and is mainly due  
455 to their correlations with  $n_{sw}$ . If the effect of  $n_{sw}$  is removed, this peak will diminish or disappear.

456 The ranking presented in Table 1 can be useful for modeling radiation belt electrons. The  
457 table may help modelers decide which parameters need to be considered as inputs to their models.

458

## 459 **5. Discussion**

### 460 **5.1 Untangling the solar wind and magnetospheric drivers**

461 An important factor that is often ignored and underappreciated in many solar wind-  
462 magnetosphere interaction studies is that many solar wind parameters positively or negatively  
463 correlate with one another, which may introduce complications and ambiguities in the causal-effect  
464 interpretation of the data. In the present study, we use conditional mutual information, CMI, to  
465 untangle the effects of the solar wind and magnetospheric drivers of the radiation belt electrons  
466 PSD having  $\mu = 725\text{--}875$  MeV  $G^{-1}$  and  $K = 0.09\text{--}0.13$   $R_E G^{-0.5}$  (average energy  $\sim 1.6$  MeV).

467 The radiation belt electron response time lags to  $V_{sw}$ ,  $n_{sw}$ , AL, and SYM-H obtained from

468 correlational analysis differ from those obtained from CMIs that have removed the effect of the  
469  $V_{sw}$  or  $n_{sw}$  as summarized in Table 2 (from Figures 2, 10, and 12). For the purpose of facilitating  
470 a more precise comparison, Table 2 lists only the peak  $\tau$  even if the peak may be broad whereas  
471 Table 1 lists a range of  $\tau$ , if the peak is broad. The response lag times obtained by CMIs are  
472 deemed more accurate because the effect of  $V_{sw}$  or  $n_{sw}$  has been removed. For example,  $\text{CMI}(n_{sw}$   
473  $\rightarrow \text{PSD} | V_{sw})$  peaks at  $t = 7\text{--}11$  hr whereas  $\text{corr}(n_{sw} \rightarrow \text{PSD})$  has a minimum at  $\tau = 15$  hr (*Lyatsky*  
474 *and Khazanov, 2008*). The smaller  $\tau$  is deemed a more accurate time scale for magnetopause  
475 shadowing, which physically makes sense and is consistent with observations (e.g., *Turner et*  
476 *al., 2014a; Xiang et al., 2017; 2018; Turner and Ukhorskiy, 2020*). The shift in the peak CMI  
477 depends on the conditional variable  $z$  in the  $\text{CMI}(x \rightarrow y | z)$ . If the (linear and nonlinear) correlation  
478 of  $z$  with  $y$  is smaller than that between  $x$  and  $y$ , then removing the effect of  $z$  would shift the peak  
479 to a larger value and vice versa.

480 The response of the radiation belt electrons to  $n_{sw}$  has dual mode. At small  $\tau$ ,  $n_{sw}$  negatively  
481 correlates with the electron PSD with a peak response time at  $\tau = 7\text{--}11$  hr, which can be attributed  
482 to the magnetopause shadowing effect. However, at large  $\tau$  ( $\tau > 80$  hr),  $n_{sw}$  positively correlates  
483 with the electron PSD as shown in Figures 2e and 3. It is not clear what causes this positive  
484 correlation.  $n_{sw}$  may be a proxy for another solar wind parameter. An increase in  $n_{sw}$  is sometimes  
485 accompanied by  $n_{sw}$  fluctuations, which can drive ULF waves in the magnetosphere and accelerate  
486 electrons (e.g., *Kepko and Viall, 2019, Ukhorskiy et al., 2005*). Whichever parameter drives the  
487 electron acceleration, the result suggests a rather slow process for electron acceleration,  $\tau > 80$  hr.  
488 This will be investigated in our follow up study.

489

## 490 **5.2 The radial dependences of the radiation belt electrons**

491 The responses of radiation belt electrons to  $V_{sw}$ ,  $n_{sw}$ ,  $P_{dyn}$ , AL, and SYM-H have radial  
492 dependence. The data coverage for the electrons with  $\mu = 725\text{--}875$  MeV  $G^{-1}$  and  $K = 0.09\text{--}0.13$   
493  $R_E G^{-0.5}$  is poor for  $L^* < 3$  and  $L^* > 6.5$ . Hence, the present study does not consider these  $L^*$   
494 ranges. The effect of  $n_{sw}$  and  $P_{dyn}$  on the radiation belt electron PSD appear to be significant only  
495 at  $L^* = 4.5\text{--}6$  and insignificant at  $L^* = 3\text{--}4.5$ . This suggests that the magnetopause shadowing is  
496 effective mostly at  $L^* = 4.5\text{--}6$ . At  $L^* = 6\text{--}6.5$ , there is a high variability in PSD and the bin has  
497 the fewest number of points ( $n = 336$ ) and hence the result is deemed unreliable. In contrast, the  
498 effect of  $V_{sw}$  on the electron PSD appears to be significant at a larger range of  $L^*$ ,  $L^* = 3.5$  to  $6.5$ .

499 An increase in  $n_{sw}$  or  $P_{dyn}$  compresses the magnetosphere leading to the electron loss at  
500 high  $L^*$ , e.g.,  $L^* > 7$ . However, ULF waves generated throughout the magnetosphere due to the  
501 compression would redistribute the loss to lower  $L^*$ . Our result shows that the electron loss can  
502 be seen at  $L^* = 4.5\text{--}6$ , consistent with understanding from observations and simulations (*Turner*  
503 *et al.* 2012, 2014a; *Xiang et al.* 2017; 2018; *Turner and Ukhorskiy*, 2020). At higher  $L^*$ , the noise  
504 in the  $CMI(n_{sw} \rightarrow PSD | V_{sw})$  is higher, which can be attributed to higher variability of the PSD.  
505 For example, the PSD initially decreases due to the magnetopause compression and then increase  
506 because of the outward diffusion (*Turner et al.*, 2012; *Shprits et al.*, 2006). Our result differs from  
507 Zhao et al. (2017) that found that  $P_{dyn}$  negatively correlates with PSD only at a small range of  $L^*$   
508 band near 6 (see their Figure 4c).

509 The radiation belt electrons also have strong dependences on the internal state of the  
510 magnetosphere. In the present study, this is explored and exemplified with AL and SYM-H, which  
511 can be used as proxies for magnetospheric state. However, the dependences on AL and SYM-H  
512 vary with radial distance or  $L^*$ . The dependence of the radiation belt electrons on AL is significant  
513 at  $L^* = 4\text{--}6$  while the dependence on SYM-H is significant at  $L^* = 3\text{--}6$ . The response of the

514 radiation belt electrons to AL and SYM-H peak at  $\tau = 40\text{--}80$  and  $\tau = 20\text{--}60$  hr, respectively. These  
515 lag times are averaged for all  $L^*$ , but the smaller  $\tau$  for SYM-H can also be seen when the data are  
516 binned by  $L^* = 0.5$  (Figures 11 and 13). This difference in response lag times are also seen in the  
517  $\text{corr}(\text{AL} \rightarrow \text{PSD})$  and  $\text{corr}(\text{SYM-H} \rightarrow \text{PSD})$  in Zhao et al. (2017), but their peak  $\tau$  are smaller,  
518 which may be attributed, at least partly, to their usage of daily resolution data and their correlations  
519 did not remove the effect of  $V_{sw}$ . The responses to AL and SYM-H are discussed further in Section  
520 5.3.

521

### 522 **5.3 Implications to electron acceleration mechanism and transport**

523 One of the fundamental questions in radiation belt physics is how the electrons are  
524 accelerated to relativistic energies ( $> 1$  MeV). There have been many proposed mechanisms, but  
525 most tend to fall into two categories: (1) local acceleration and (2) radial transport (see review in  
526 Friedel et al., 2002).

527 In the local acceleration mechanism, substorms or storms transport low energy electrons (a  
528 few to tens of keVs) from the plasma sheet into the inner magnetosphere, which are often referred  
529 to as the source population (e.g., *Baker et al.*, 1996; *Tang et al.*, 2017; *Boyd et al.*, 2016). The  
530 temperature anisotropy in the source population leads to the growth of the VLF whistler mode  
531 chorus waves (e.g., *Meredith et al.*, 2001; *W. Li et al.*, 2009). Substorms and storms also transport  
532 high energy electrons (a few tens to hundreds keVs) electrons from the plasma sheet into the inner  
533 magnetosphere, which are commonly referred to as seed population. Then, the chorus waves  
534 interact with the seed electrons and energize them to relativistic energies (e.g., *Summers et al.*,  
535 1998; 2002; *Horne et al.*, 2005; Thorne, 2010; Reeves et al., 2013; *W. Li et al.*, 2014).

536 In the radial transport acceleration mechanism, electrons at larger  $L^*$  get accelerated as

537 they move inward to the inner magnetosphere through interactions with ULF waves (e.g., *Baker*  
538 *et al.*, 1998; *Li and Temerin*, 2001; *Li et al.*, 2005; *Ukhorskiy et al.*, 2005; *Mathie and Mann*, 2000;  
539 *Elkington et al.*, 1999; *Kepko and Viall*, 2019). These ULF waves can be associated with high  $V_{sw}$   
540 and Kelvin-Helmholtz Instability (KHI) or  $n_{sw}$  or  $P_{dyn}$  fluctuations (e.g., *Johnson et al.*, 2014;  
541 *Engebretson et al.*, 1998; *Vennerstrøm*, 1999; *Claudepierre et al.*, 2010; *Takahashi and Ukhorskiy*,  
542 2007; *Liu et al.*, 2010).

543 The result of  $CMI(V_{sw} \rightarrow PSD | n_{sw})$  as a function of  $L^*$  (Figures 8 and 9) can be interpreted  
544 in terms of local acceleration mechanism. Figure 9 shows that the radiation belt electrons at  $L^* =$   
545 4.5–5.5 have the shortest response lag time with peak  $\tau = 35$ –50 hr and the highest significance.  
546 The response lag time is larger and broader at higher  $L^*$ ,  $\tau = 45$ –65 hr ( $L^* = 5.5$ –6),  $\tau = 40$ –100  
547 hr ( $L^* = 6$ –6.5), and at lower  $L^*$ ,  $\tau = 35$ –55 hr ( $L^* = 4$ –4.5) and  $\tau = 45$ –60 hr ( $L^* = 3.5$ –4). This  
548 would suggest that local acceleration peaks at  $L^* = 4.5$ –5.5 and the shifting of the peak to a larger  
549  $\tau$  at higher or lower  $L^*$  suggests outward or inward diffusion, respectively.

550 Previous studies also found evidence for local acceleration at this  $L^*$  band by examining  
551 the MeV PSD or electron fluxes as a function of radial distance (*Green and Kivelson*, 2004) or  
552 microburst MeV electron precipitation (*O'Brien et al.*, 2003). More recently, in the RBSP era,  
553 *Tang et al.* (2017) found evidence of local acceleration of 1 MeV electrons at  $L \sim 4$ –5 in 74 storm  
554 events. *Boyd et al.* (2018) found the peak PSD is located mostly at  $L^* = 4.5$  – 5.5 in 80 storm  
555 events. They concluded that 70 out of 80 events show evidence of local acceleration based on the  
556 PSD vs.  $L^*$  spectra.

557 However, there is also evidence that suggests localized acceleration in tandem with  
558 outward or inward diffusion originating from  $L^* = 4.5$ –5.5 (e.g., *Allison and Shprits*, 2020). For  
559 example, at  $L^* = 4$ –4.5, one can see that the  $i_{tr}$  starts increasing at  $\tau = 25$  hr, very much about the

560 same time  $i_{tr}$  increases at  $L^* = 4.5\text{--}5.5$  hr, but the significance is lower (Figure 8). This may  
561 suggest that the whistler mode chorus waves are also present at  $L^* = 4\text{--}4.5$  and not all 1–2 MeV  
562 electrons are transported from  $L^* = 4.5\text{--}5.5$ . The same dynamics can be seen at the outermost  $L^*$ ,  
563  $L^* = 6\text{--}6.5$ .

564 The radial diffusion time scale can be estimated from the peak  $\tau$  at each  $L^*$  band. In Figure  
565 9, the peak  $\tau$  increases from  $\sim 40$  hr at  $L^* = 4.5\text{--}5.5$  to  $\sim 60$  hr at  $L^* = 5.5\text{--}6$ , suggesting outward  
566 diffusion time scale of 40 hr per  $R_E$ . The diffusion time scale of 40 hr (or about 2 days) per  $R_E$  can  
567 be compared with the theoretical estimate of 1–6 days that is attributed to ULF waves at  $L^* = 6$   
568 (e.g., *Elkington et al.*, 2003).

569 Although the present study does not rule out the ULF waves and radial transport as the  
570 acceleration source and such mechanism is certainly operational in some or many cases, the local  
571 acceleration signature appears to be dominant statistically.

572 Our interpretation of local acceleration and time scale based on the information theoretic  
573 analysis of the observations can be complemented and strengthened with physics-based modeling  
574 (e.g., *Shprits et al.* 2009; *Reeves et al.*, 2012; *Horne et al.*, 2013; *Camporeale et al.*, 2013; 2016).  
575 It would be interesting to analyze the simulation data using CMI in a similar manner done in the  
576 present study.

577 The result of  $\text{CMI}(\text{AL} \rightarrow \text{PSD} | V_{sw})$  can also be interpreted as consistent with local  
578 acceleration at  $L^* = 4\text{--}5.5$  and inward and outward diffusion to lower and higher  $L^*$ , respectively.  
579 This may not be too surprising because the link between  $V_{sw}$  and PSD involves substorm injections.

580 *Iles et al.* (2006) examined a substorm event and found that peak PSD for electrons  $> 0.8$   
581 MeV is located at  $L^* = 4.3\text{--}5.5$ , which is close to the  $L^*$  band with the largest CMI significance,  
582  $L^* = 4.5\text{--}5.5$ . They also found evidence of local acceleration and radial diffusion.

583           The radiation belt electron response lag time appears more complicated for CMI(SYM-H  
584 → PSD|  $V_{sw}$ ) (Figure 13). The peak  $\tau$  is most significant and smallest at  $L^* = 5-5.5$  suggesting  
585 local acceleration peaks at this  $L^*$  band. There is evidence for inward and outward diffusion from  
586 this  $L^*$  band. However, there is also evidence for local acceleration at smaller  $L^*$ . The  
587 complication may stem from the competing processes that would increase and decrease PSD and  
588 electron fluxes. A decrease of SYM-H would indicate increase in the ring current and the intensity  
589 of storms. The general response to storm plasma injections would be an increase in whistler mode  
590 chorus waves and electron acceleration, leading to an increase in PSD. However, storm would  
591 increase the ring current, which would reduce  $|B|$ . This would cause outward diffusion and  
592 reduction of PSD as the electrons would attempt to conserve the third adiabatic invariant (*Turner*  
593 *et al.*, 2012). This  $D_{st}$  or SYM-H effect would be stronger with increasing radial distance because  
594 magnetospheric  $|B|$  decreases with  $r^{-3}$ . This could be a contributing factor in the high noise and  
595 variability seen in  $L^* = 6-6.5$ . Studies have shown that the radiation belt electron response at the  
596 outermost  $L^*$  band can sometimes be enhancement, depletion, or no change (*O'Brien et al.*, 2001;  
597 *Reeves et al.*, 2003). These competing processes may contribute to this variability in the radiation  
598 belt response. Also, different types of storms would affect different  $L^*$  differently. For example,  
599 *Turner et al* (2019) reported that full coronal mass ejection (CME) storms cause MeV electron  
600 enhancements at  $L < \sim 5$  while stream interaction region (SIR) storms cause enhancements at  $L >$   
601  $\sim 4.5$ . CME sheaths and CME ejecta can cause depletions throughout the outer radiation belt.

602           Comparisons of Figures 11 and 13 show that response lag time ( $\tau$ ) for SYM-H (Figure 13)  
603 is smaller than that for AL by about 9–10 hr (Figure 11). Our interpretation is that in both cases  
604 particle injections lead to local accelerations. During storm time, on average, the peak of the main  
605 phase (minimum SYM-H) is reached about 9 hr after the start of the main phase (start of particle

606 injection) (Yokoyama and Kamide, 1997; Fok et al., 2011). On the other hand, AL is a proxy for  
607 the auroral electrojets and their peak enhancement (minimum AL) can be reached fairly quickly  
608 from the time of substorm injections, within minutes. Thus, the smaller response time scale seen  
609 for SYM-H (Figure 13) may be attributed to the relative time scale for electron acceleration to  
610 MeV energy range and SYM-H reaching its minimum from the start of particle injection. As  
611 mentioned above, it would be useful to confirm this with a physics-based modeling study (e.g.,  
612 *Shprits et al. 2009; Reeves et al., 2012; Horne et al., 2013; Camporeale et al., 2013; 2016*)

613

#### 614 **5.4 Ranking of the solar wind and magnetospheric drivers**

615 We rank the solar wind and magnetospheric parameters based on the information transfer  
616 to the radiation belt electron PSD. This ranking can be useful for modelers who would like to  
617 develop models that input solar wind and magnetospheric parameters and predict radiation belt  
618 electrons having energies 1–2 MeV. This is shown in Table 1. The table shows that  $V_{sw}$  transfers  
619 the most information to the radiation belt electrons and hence should be considered an important,  
620 if not the most important, input parameter to radiation belt models. However, SYM-H can also be  
621 an important input parameter for models for two reasons: (1) SYM-H transfers the second most  
622 information to the radiation belt electrons; and (2) Out of a long list of parameters ( $V_{sw}$ ,  $n_{sw}$ ,  $P_{dyn}$ ,  
623 AL, SYM-H), only SYM-H has information the radiation belt electrons at  $L^* = 3-3.5$  albeit only  
624 a small amount of information. SYM-H can play a crucial role for models that predict the radiation  
625 belt electrons at  $L^* = 3-3.5$ .

626

#### 627 **6. Summary**

628 The following summarizes the main results of our study.

- 629 • CMI can be a powerful tool to untangle the effect of solar wind and magnetospheric drivers of  
630 the radiation belt electrons.
- 631 • Pearson correlations give lag times that are different than those obtained using CMI that  
632 removes the effect of another driver. Table 2 shows some of the comparisons. For example,  
633  $CMI(n_{sw} \rightarrow PSD | V_{sw})$  peaks at  $\tau = 7-11$  hr, whereas  $|\text{corr}(n_{sw} \rightarrow PSD)|$  peaks at  $\tau = 15$  hr. The  
634 smaller response lag time of 7-11 hr physically makes more sense because the magnetopause  
635 shadowing process should be quick.
- 636 • There is a long-range positive correlation between  $n_{sw}$  and PSD at  $\tau = 80-120$  hr.
- 637 • The magnetopause shadowing effect is only significant at  $L^* = 4.5-6$ .
- 638 • The effect of  $V_{sw}$  is significant at  $L^* = 3.5-6.5$ .
- 639 • The analysis of  $V_{sw}$ , AL, and SYM-H as a function of  $L^*$  can be interpreted in terms of local  
640 acceleration and subsequent inward and outward diffusion.
- 641 • Table 1 ranks solar wind and magnetospheric parameters based on information transfer to the  
642 radiation belt electron PSD.

643

644

645

646 **Acknowledgments.** The solar wind, SYM-H, and AL dataset were obtained from NASA  
647 OMNIweb <https://omniweb.gsfc.nasa.gov/>. All RBSP-ECT data are publicly available at the  
648 website <http://www.rbsp-ect.lanl.gov>. All the derived data products in this paper are publicly  
649 available at the Zenodo Archive (Wing, 2021). Simon Wing acknowledges support of NASA Van  
650 Allen Probe Contract NNN16AA09T and NASA Grants NNX16AQ87G, 80NSSC20K0704,  
651 80NSSC19K0843, 80NSSC19K0822, 80NSSC20K0188, 80NSSC20K1279, and

652 80NSSC20K1271. Drew Turner is thankful for funding from NASA grants 80NSSC19K0280 and  
653 80NSSC18K1377. This work has benefitted from discussions within the International Space  
654 Science Institute (ISSI) Team # 455 “Complex Systems Perspectives Pertaining to the Research  
655 of the Near-Earth Electromagnetic Environment.”

656

657

658  
659  
660  
661  
662  
663  
664  
665  
666  
667  
668  
669  
670  
671  
672  
673  
674  
675  
676  
677  
678  
679  
680

## References

Allison, H.J., Shprits, Y. Y. (2020), Local heating of radiation belt electrons to ultra-relativistic energies. *Nat Commun* **11**, 4533, <https://doi.org/10.1038/s41467-020-18053-z>

Baker, D. N., R. L. McPherron, T. E. Cayton, and R. W. Klebesadel (1990), Linear prediction filter analysis of relativistic electron properties at 6.6  $R_E$ , *J. Geophys. Res.*, 95(A9),15133–15140, doi:[10.1029/JA095iA09p15133](https://doi.org/10.1029/JA095iA09p15133).

Baker, D. N., Pulkkinen, T. I., Angelopoulos, V., Baumjohann, W., and McPherron, R. L. (1996), Neutral line model of substorms: Past results and present view, *J. Geophys. Res.*, 101( A6), 12975– 13010, doi:[10.1029/95JA03753](https://doi.org/10.1029/95JA03753).

Baker, D. N., X Li, J. B Blake, S. Kanekal (1998), Strong electron acceleration in the Earth's magnetosphere, *Adv. Space Res.*, 21, 609-613, doi:10.1016/S0273-1177(97)00970-8.

Baker, D. N., et al. (2012), The Relativistic Electron-Proton Telescope (REPT) Instrument on Board the Radiation Belt Storm Probes (RBSP) Spacecraft: Characterization of Earth's Radiation Belt High-Energy Particle Populations, *Space Sci. Rev.*, doi:10.1007/s11214-012-9950-9.

Baker, D.N., Erickson, P.J., Fennell, J.F. *et al.* Space Weather Effects in the Earth's Radiation Belts. *Space Sci Rev* **214**, 17 (2018). <https://doi.org/10.1007/s11214-017-0452-7>

Baker, D. N., Hoxie, V., Zhao, H., Jaynes, A. N., Kanekal, S., Li, X., & Elkington, S. (2019a). Multiyear measurements of radiation belt electrons: Acceleration, transport, and loss. *Journal of Geophysical Research: Space Physics*, 124, 2588– 2602. <https://doi.org/10.1029/2018JA026259>

Baker, D. N., Zhao, H., Li, X., Kanekal, S. G., Jaynes, A. N., Kress, B. T., et al. (2019b). Comparison of Van Allen Probes Energetic Electron Data with corresponding GOES-15

681 Measurements: 2012–2018. *Journal of Geophysical Research: Space Physics*, 124,  
682 <https://doi.org/10.1029/2019JA027331>

683 Balasis, G., Daglis, I. A., Papadimitriou, C., Kalimeri, M., Anastasiadis, A., and Eftaxias,  
684 K. (2009), Investigating dynamical complexity in the magnetosphere using various entropy  
685 measures, *J. Geophys. Res.*, 114, A00D06, doi:[10.1029/2008JA014035](https://doi.org/10.1029/2008JA014035).

686 Balasis, G.; Donner, R.V.; Potirakis, S.M.; Runge, J.; Papadimitriou, C.; Daglis, I.A.; Eftaxias, K.;  
687 Kurths (2013), J. Statistical mechanics and information-theoretic perspectives on complexity  
688 in the Earth system. *Entropy*, 15, 4844–4888, doi:10.3390/e15114844.

689 Balikhin, M. A., R. J. Boynton, S. A. Billings, M. Gedalin, N. Ganushkina, D. Coca, and H.  
690 Wei (2010), Data based quest for solar wind-magnetosphere coupling function, *Geophys.*  
691 *Res. Lett.*, 37, L24107, doi:[10.1029/2010GL045733](https://doi.org/10.1029/2010GL045733).

692 Balikhin, M. A., R. J. Boynton, S. N. Walker, J. E. Borovsky, S. A. Billings, and H. L.  
693 Wei(2011), Using the NARMAX approach to model the evolution of energetic electrons  
694 fluxes at geostationary orbit, *Geophys. Res. Lett.*, 38, L18105, doi:[10.1029/2011GL048980](https://doi.org/10.1029/2011GL048980).

695 Blake, J.B., Carranza, P.A., Claudepierre, S.G. *et al.* *The Magnetic Electron Ion*  
696 *Spectrometer (MagEIS) Instruments Aboard the Radiation Belt Storm Probes (RBSP)*  
697 *Spacecraft. Space Sci Rev* **179**, 383–421 (2013). [https://doi.org/10.1007/s11214-013-9991-](https://doi.org/10.1007/s11214-013-9991-8)  
698 8

699 Borovsky, J. E. (2017). Time-integral correlations of multiple variables with the relativistic-  
700 electron flux at geosynchronous orbit: The strong roles of substorm-injected electrons and  
701 the ion plasma sheet. *Journal of Geophysical Research: Space*  
702 *Physics*, 122, 11,961– 11,990. <https://doi.org/10.1002/2017JA024476>

703 Borovsky, J. E. (2018), On the origins of the intercorrelations between solar wind  
704 variables. *Journal of Geophysical Research: Space Physics*, 123, 20– 29. <https://doi.org/10.1002/2017JA024650>  
705

706 Borovsky, J. E. (2020), What magnetospheric and ionospheric researchers should know about the  
707 solar wind, *J. Atmos. Sol. Phys.*, 204, 105271, <https://doi.org/10.1016/j.jastp.2020.105271>.

708 Boyd, A. J., Spence, H. E., Claudepierre, S. G., Fennell, J. F., Blake, J. B., Baker, D. N., Reeves,  
709 G. D., and Turner, D. L. (2014), Quantifying the radiation belt seed population in the March  
710 17, 2013 electron acceleration event, *Geophys. Res. Lett.*, 41, 2275– 2281,  
711 doi:[10.1002/2014GL059626](https://doi.org/10.1002/2014GL059626).

712 Boyd, A. J., Spence, H. E., Huang, C.-L., Reeves, G. D., Baker, D. N., Turner, D. L., Claudepierre,  
713 S. G., Fennell, J. F., Blake, J. B., and Shprits, Y. Y. (2016), Statistical properties of the  
714 radiation belt seed population, *J. Geophys. Res. Space Physics*, 121, 7636– 7646,  
715 doi:[10.1002/2016JA022652](https://doi.org/10.1002/2016JA022652).

716 Boyd, A. J., Turner, D. L., Reeves, G. D., Spence, H. E., Baker, D. N., & Blake, J. B. (2018). What  
717 causes radiation belt enhancements: A survey of the Van Allen Probes Era. *Geophysical*  
718 *Research Letters*, 45, 5253– 5259. <https://doi.org/10.1029/2018GL077699>

719 Boyd, A. J., Spence, H. E., Reeves, G. D., Funsten, H. O., Skoug, R. M., Larsen, B. A., et al.  
720 (2021). RBSP-ECT combined pitch angle resolved electron flux data product. *Journal of*  
721 *Geophysical Research: Space Physics*, 126,  
722 e2020JA028637. <https://doi.org/10.1029/2020JA028637>

723 Camporeale, E., Delzanno, G. L., Zaharia, S., and Koller, J. (2013), On the numerical simulation  
724 of particle dynamics in the radiation belt: 1. Implicit and semi-implicit schemes, *J. Geophys.*  
725 *Res. Space Physics*, 118, 3463– 3475, doi:[10.1002/jgra.50293](https://doi.org/10.1002/jgra.50293).

726 Camporeale, E., Shprits, Y., Chandorkar, M., Drozdov, A., and Wing, S. (2016), On the  
727 propagation of uncertainties in radiation belt simulations, *Space*  
728 *Weather*, 14, 982–992, doi:[10.1002/2016SW001494](https://doi.org/10.1002/2016SW001494)

729 Claudepierre, S. G., M. K. Hudson, W. Lotko, J. G. Lyon, and R. E. Denton (2010), Solar wind  
730 driving of magnetospheric ULF waves: Field line resonances driven by dynamic pressure  
731 fluctuations, *J. Geophys. Res.*, 115, A11202, doi:[10.1029/2010JA015399](https://doi.org/10.1029/2010JA015399).

732 Consolini, G., R. Tozzi, and P. De Michelis (2009), Complexity in the sunspot cycle, *A&A* 506,  
733 1381–1391, DOI: 10.1051/0004-6361/200811074

734 Davis, T. N., and Sugiura, M. (1966), Auroral electrojet activity index *AE* and its universal time  
735 variations, *J. Geophys. Res.*, 71(3), 785–801, doi:[10.1029/JZ071i003p00785](https://doi.org/10.1029/JZ071i003p00785).

736 Darbellay, G. A., and I. Vajda (1999), Estimation of the Information by an Adaptive Partitioning  
737 of the Observations Space, *IEEE Transactions on Information Theory*, 45, 1315–1321.

738 Dessler, A., and E. Parker (1959), Hydromagnetic theory of geomagnetic storms, *J. Geophys.*  
739 *Res.*, 64(12), 2239–2252, doi:[10.1029/JZ064i012p02239](https://doi.org/10.1029/JZ064i012p02239).

740 Elkington, S. R., M. K. Hudson, and A. A. Chan (1999), Acceleration of relativistic electrons via  
741 drift-resonant interaction with toroidal-mode Pc-5 ULF oscillations, *Geophys. Res. Lett.*, 26,  
742 3273.

743 Elkington, S. R., Hudson, M. K., and Chan, A. A. (2003), Resonant acceleration and diffusion of  
744 outer zone electrons in an asymmetric geomagnetic field, *J. Geophys. Res.*, 108, 1116,  
745 doi:[10.1029/2001JA009202](https://doi.org/10.1029/2001JA009202)

746 Engebretson, M., K.-H. Glassmeier, M. Stellmacher, W. J. Hughes, and H. Lühr (1998), The  
747 dependence of high-latitude PcS wave power on solar wind velocity and on the phase of

748 high-speed solar wind streams, *J. Geophys. Res.*, 103(A11), 26271–26283,  
749 doi:[10.1029/97JA03143](https://doi.org/10.1029/97JA03143).

750 Fok, M.-C., Moore, T. E., Slinker, S. P., Fedder, J. A., Delcourt, D. C., Nosé, M., and Chen, S.-  
751 H. (2011), Modeling the superstorm in November 2003, *J. Geophys. Res.*, 116, A00J17,  
752 doi:[10.1029/2010JA015720](https://doi.org/10.1029/2010JA015720).

753 Friedel, R. H. W., G. D. Reeves, and T. Obara (2002), Relativistic electron dy-  
754 namics in the inner magnetosphere—A review, *J. Atmos. Sol. Terr. Phys.*, 64, 265.

755 Green, J. C., and M. G. Kivelson (2004), Relativistic electrons in the outer radiation belt:  
756 Differentiating between acceleration mechanisms, *J. Geophys. Res.*, 109, A03213,  
757 doi:[10.1029/2003JA010153](https://doi.org/10.1029/2003JA010153).

758 Horne, R. B., R. M. Thorne, S. A. Glauert, J. M. Albert, N. P. Meredith, and R. R. Anderson  
759 (2005), Timescale for radiation belt electron acceleration by whistler mode chorus waves, *J.*  
760 *Geophys. Res.*, 110, A03225, doi:[10.1029/2004JA010811](https://doi.org/10.1029/2004JA010811)

761 Horne, R. B., Glauert, S. A., Meredith, N. P., Boscher, D., Maget, V., Heynderickx, D.,  
762 and Pitchford, D. (2013), Space weather impacts on satellites and forecasting the Earth's  
763 electron radiation belts with SPACECAST, *Space Weather*, 11, 169–186,  
764 doi:[10.1002/swe.20023](https://doi.org/10.1002/swe.20023).

765 Iles, R. H. A., Meredith, N. P., Fazakerley, A. N., and Horne, R. B. (2006), Phase space density  
766 analysis of the outer radiation belt energetic electron dynamics, *J. Geophys. Res.*, 111,  
767 A03204, doi:[10.1029/2005JA011206](https://doi.org/10.1029/2005JA011206).

768 Iyemori, T. (1990), Storm-time magnetospheric currents inferred from mid-latitude geomagnetic  
769 field variations, *J. Geomag. Geoelectr.*, 42, 1249–1265.

770 Johnson, J. R., and S. Wing (2005), A solar cycle dependence of nonlinearity in magnetospheric  
771 activity, *J. Geophys. Res.*, 110, A04211, doi:[10.1029/2004JA010638](https://doi.org/10.1029/2004JA010638).

772 Johnson, J. R., and S. Wing (2014), External versus internal triggering of substorms: An  
773 information-theoretical approach, *Geophys. Res. Lett.*, 41, 5748–5754,  
774 doi:[10.1002/2014GL060928](https://doi.org/10.1002/2014GL060928).

775 Johnson, J. R., S. Wing, and P. A. Delamere (2014), Kelvin Helmholtz Instability in Planetary  
776 Magnetospheres, *Space Sci. Rev.*, 184, 1 – 31, doi:10.1007/s11214-014-0085-z.

777 Johnson, J. R., Wing, S., and Camporeale, E. (2018), Transfer entropy and cumulant-based cost as  
778 measures of nonlinear causal relationships in space plasmas: applications to  $D_{st}$ , *Ann.*  
779 *Geophys.*, 36, 945-952, <https://doi.org/10.5194/angeo-36-945-2018>

780 Katus, R. M., Liemohn, M. W., Gallagher, D. L., Ridley, A., and Zou, S. (2013), Evidence for  
781 potential and inductive convection during intense geomagnetic events using normalized  
782 superposed epoch analysis, *J. Geophys. Res. Space Physics*, 118, 181– 191,  
783 doi:[10.1029/2012JA017915](https://doi.org/10.1029/2012JA017915).

784 Kellerman, A. C., and Y. Y. Shprits (2012), On the influence of solar wind conditions on the outer-  
785 electron radiation belt, *J. Geophys. Res.*, 117, A05217, doi:[10.1029/2011JA017253](https://doi.org/10.1029/2011JA017253).

786 Kepko, L., & Viall, N. M. (2019). The source, significance, and magnetospheric impact of periodic  
787 density structures within stream interaction regions. *Journal of Geophysical Research: Space*  
788 *Physics*, 124, 7722– 7743. <https://doi.org/10.1029/2019JA026962>

789 Lejosne, S., Kollmann, P. Radiation Belt Radial Diffusion at Earth and Beyond. *Space Sci*  
790 *Rev* **216**, 19 (2020). <https://doi.org/10.1007/s11214-020-0642-6>

791 Li, W. (1990), Mutual Information Functions Versus Correlation Functions, *J. Stat. Phys.*, 60, 823–  
792 837.

793 Li, W., Thorne, R. M., Angelopoulos, V., Bonnell, J. W., McFadden, J. P., Carlson, C.  
794 W., LeContel, O., Roux, A., Glassmeier, K. H., and Auster, H. U. (2009), Evaluation of  
795 whistler-mode chorus intensification on the nightside during an injection event observed on  
796 the THEMIS spacecraft, *J. Geophys. Res.*, 114, A00C14, doi:[10.1029/2008JA013554](https://doi.org/10.1029/2008JA013554).

797 Li, W., et al. (2014), Radiation belt electron acceleration by chorus waves during the 17 March  
798 2013 storm, *J. Geophys. Res. Space Physics*, 119, 4681–4693, doi:[10.1002/2014JA019945](https://doi.org/10.1002/2014JA019945).

799 Li, X., and M. A. Temerin (2001), The electron radiation belt, *Space Sci. Rev.*, 95, 569 - 580.

800 Li, X., M. Temerin, D. Baker, G. Reeves, and D. Larson (2001), Quantitative prediction of  
801 radiation belt electrons at geostationary orbit based on solar wind measurements, *Geophys.*  
802 *Res. Lett.*, **28**(9), 1887–1890.

803 Li, X., D. N. Baker, M. Temerin, G. Reeves, R. Friedel, and C. Shen (2005), Energetic electrons,  
804 50 keV to 6 MeV, at geosynchronous orbit: Their responses to solar wind variations, *Space*  
805 *Weather*, 3, S04001, doi:[10.1029/2004SW000105](https://doi.org/10.1029/2004SW000105).

806 Li, X., Barker, A. B., Baker, D. N., Tu, W. C., Sarris, T. E., Selesnick, R. S., Friedel, R., and Shen,  
807 C. (2009), Modeling the deep penetration of outer belt electrons during the “Halloween”  
808 magnetic storm in 2003, *Space Weather*, 7, S02004, doi:[10.1029/2008SW000418](https://doi.org/10.1029/2008SW000418).

809 Liu, W., Sarris, T. E., Li, X., Ergun, R., Angelopoulos, V., Bonnell, J., and Glassmeier, K.  
810 H. (2010), Solar wind influence on Pc4 and Pc5 ULF wave activity in the inner  
811 magnetosphere, *J. Geophys. Res.*, 115, A12201, doi:[10.1029/2010JA015299](https://doi.org/10.1029/2010JA015299).

812 Lyatsky, W., and G. V. Khazanov (2008), Effect of solar wind density on relativistic electrons at  
813 geosynchronous orbit, *Geophys. Res. Lett.*, 35, L03109, doi:[10.1029/2007GL032524](https://doi.org/10.1029/2007GL032524).

814 Maggiolo, R., Hamrin, M., De Keyser, J., Pitkänen, T., Cessateur, G., Gunell, H., & Maes, L.  
815 (2017). The delayed time response of geomagnetic activity to the solar wind. *Journal of*

816 Geophysical Research: Space Physics, 122, 11,109– 11,127.  
817 <https://doi.org/10.1002/2016JA023793>

818 March, T. K., Chapman, S. C., and Dendy, R. O. (2005), Mutual information between  
819 geomagnetic indices and the solar wind as seen by WIND: Implications for propagation time  
820 estimates, *Geophys. Res. Lett.*, 32, L04101, doi:[10.1029/2004GL021677](https://doi.org/10.1029/2004GL021677).

821 Mathie, R. A., & Mann, I. R. (2000). A correlation between extended intervals of ULF wave power  
822 and stormtime geosynchronous relativistic electron flux enhancements. *Geophysical*  
823 *Research Letters*, 27(20), 3261–3264. <https://doi.org/10.1029/2000gl003822>

824 Manshour,P., Balasis,G.; Consolini, G.; Papadimitriou, C., Paluš, M. (2021), Causality and  
825 Information Transfer Between the Solar Wind and the Magnetosphere–Ionosphere System.  
826 *Entropy*, 23, 390. <https://doi.org/10.3390/e23040390>

827 Mathie, R. A., and I. R. Mann (2000), A correlation between extended intervals of ULF wave  
828 power and storm-time geosynchronous relativistic electron flux enhancements, *Geophys.*  
829 *Res. Lett.*, 27, 3621–3264, doi:[10.1029/2000GL003822](https://doi.org/10.1029/2000GL003822).

830 Mathie, R. A., and I. R. Mann (2001), On the solar wind control of Pc5 ULF pulsation power at  
831 mid-latitudes: Implications for MeV electron acceleration in the outer radiation belt, *J.*  
832 *Geophys. Res.*, 106(A12), 29783–29796, doi:[10.1029/2001JA000002](https://doi.org/10.1029/2001JA000002).

833 Mauk, B. H., N. J. Fox, S. G. Kanekal, R. L. Kessel, D. G. Sibeck, and A. Ukhorskiy (2013),  
834 Science objectives and rationale for the radiation belt storm probes mission, *Space Science*  
835 *Review*, 179(1-4), 3–27, doi:[10.1007/s11214-012-9908-y](https://doi.org/10.1007/s11214-012-9908-y).

836 Meredith, N. P., Horne, R. B., and Anderson, R. R. (2001), Substorm dependence of chorus  
837 amplitudes: Implications for the acceleration of electrons to relativistic energies, *J. Geophys.*  
838 *Res.*, 106( A7), 13165– 13178, doi:[10.1029/2000JA900156](https://doi.org/10.1029/2000JA900156).

839 O'Brien, T. P., McPherron, R. L., Sornette, D., Reeves, G. D., Friedel, R., and Singer, H.  
840 J. (2001), Which magnetic storms produce relativistic electrons at geosynchronous orbit?, *J.*  
841 *Geophys. Res.*, 106( A8), 15533– 15544, doi:[10.1029/2001JA000052](https://doi.org/10.1029/2001JA000052).

842 O'Brien, T. P., Lorentzen, K. R., Mann, I. R., Meredith, N. P., Blake, J. B., Fennell, J. F., Looper,  
843 M. D., Milling, D. K., and Anderson, R. R. (2003), Energization of relativistic electrons in  
844 the presence of ULF power and MeV microbursts: Evidence for dual ULF and VLF  
845 acceleration, *J. Geophys. Res.*, 108, 1329, doi:10.1029/2002JA009784, A8.

846 Papadimitriou, Constantinos; Balasis, Georgios; Boutsis, Adamantia Z.; Daglis, Ioannis A.;  
847 Giannakis, Omiros; Anastasiadis, Anastasios; Michelis, Paola D.; Consolini, Giuseppe.  
848 (2020), Dynamical Complexity of the 2015 St. Patrick's Day Magnetic Storm at Swarm  
849 Altitudes Using Entropy Measures, *Entropy*, 22, 5, 574, <https://doi.org/10.3390/e22050574>

850 Paulikas, G. A., and J. B. Blake (1979), Effects of the solar wind on magnetospheric dynamics:  
851 Energetic electrons at the synchronous orbit, in *Quantitative Modeling of Magnetospheric*  
852 *Processes, Geophys. Monogr. Ser.*, Vol 21, pp. 180-202, AGU, Washington D.C.

853 Pinto, V. A., Kim, H.-J., Lyons, L. R., & Bortnik, J. (2018). Interplanetary parameters leading to  
854 relativistic electron enhancement and persistent depletion events at geosynchronous orbit  
855 and potential for prediction. *Journal of Geophysical Research: Space*  
856 *Physics*, 123, 1134– 1145. <https://doi.org/10.1002/2017JA024902>

857 Prichard, D., and J. Theiler (1995), Generalized redundancies for time series analysis, *Physica D:*  
858 *Non-linear Phenomena*, 84, 476–493, doi:10.1016/0167-2789(95)00041-2.

859 Reeves, G. D. (1998), Relativistic electrons and magnetic storms: 1992–1995, *Geophys. Res. Lett.*,  
860 25, 1817–1820, doi:10.1029/98GL01398.

861 Reeves, G. D., McAdams, K. L., Friedel, R. H. W., and O'Brien, T. P. (2003), Acceleration and

862 loss of relativistic electrons during geomagnetic storms, *Geophys. Res. Lett.*, 30, 1529,  
863 doi:[10.1029/2002GL016513](https://doi.org/10.1029/2002GL016513)

864 Reeves, G. D., S. K. Morley, R. H. W. Friedel, M. G. Henderson, T. E. Cayton, G. Cunningham, J.  
865 B. Blake, R. A. Christensen, and D. Thomsen (2011), On the relationship between  
866 relativistic electron flux and solar wind velocity: Paulikas and Blake revisited, *J. Geophys.*  
867 *Res.*, 116, A02213, doi:[10.1029/2010JA015735](https://doi.org/10.1029/2010JA015735).

868 Reeves, G. D., Chen, Y., Cunningham, G. S., Friedel, R. W. H., Henderson, M. G., Jordanova, V.  
869 K., Koller, J., Morley, S. K., Thomsen, M. F., and Zaharia, S. (2012), Dynamic Radiation  
870 Environment Assimilation Model: DREAM, *Space Weather*, 10, S03006,  
871 doi:[10.1029/2011SW000729](https://doi.org/10.1029/2011SW000729)

872 Reeves, G., S. Morley, and G. Cunningham (2013), Long-term variations in solar wind velocity  
873 and radiation belt electrons, *J. Geophys. Res. Space Physics*, 118, 1040–1048,  
874 doi:[10.1002/jgra.50126](https://doi.org/10.1002/jgra.50126).

875 Rigler, E. J., M. Wiltberger, and D. N. Baker (2007), Radiation belt electrons respond to multiple  
876 solar wind inputs, *J. Geophys. Res.*, 112, A06208, doi:[10.1029/2006JA012181](https://doi.org/10.1029/2006JA012181)

877 Roederer, J. G. (1970), *Dynamics of Geomagnetically Trapped Radiation*, Springer, New York,  
878 [https://doi.org/ 10.1007/978-3-642-49300-3](https://doi.org/10.1007/978-3-642-49300-3)

879 Runge, J., Balasis, G., Daglis, I.A. *et al.* Common solar wind drivers behind magnetic storm–  
880 magnetospheric substorm dependency. *Sci Rep* **8**, 16987 (2018).  
881 <https://doi.org/10.1038/s41598-018-35250-5>

882 Schulz, M., and L.J. Lanzerotti (1974) , *Particle Diffusion in the Radiation Belts*, Springer, Berlin,  
883 1974, [https:// doi.org/10.1007/978-3-642-65675-0](https://doi.org/10.1007/978-3-642-65675-0)

884 Simms, L. E., V. Pilipenko, M. J. Engebretson, G. D. Reeves, A. J. Smith, and M.

885 Clilverd (2014), Prediction of relativistic electron flux at geostationary orbit following  
886 storms: Multiple regression analysis, *J. Geophys. Res. Space Physics*, 119, 7297–7318,  
887 doi:[10.1002/2014JA019955](https://doi.org/10.1002/2014JA019955).

888 Shprits, Y. Y., R. M. Thorne, R. Friedel, G. D. Reeves, J. Fennell, D. N. Baker, and S. G.  
889 Kanekal (2006), Outward radial diffusion driven by losses at magnetopause, *J. Geophys.*  
890 *Res.*, 111, A11214, doi:[10.1029/2006JA011657](https://doi.org/10.1029/2006JA011657)

891 Shprits, Y. Y., D. A. Subbotin, N. P. Meredith, S. R. Elkington (2008), Review of modeling of  
892 losses and sources of relativistic electrons in the outer radiation belt II: Local acceleration  
893 and loss, *J. Atmos. Sol. Terr. Phys.*, 70, 1694–1713, doi:[10.1016/j.jastp.2008.06.014](https://doi.org/10.1016/j.jastp.2008.06.014).

894 Shprits, Y. Y., D. Subbotin, and B. Ni (2009), Evolution of electron fluxes in the outer radiation  
895 belt computed with the VERB code, *J. Geophys. Res.*, 114, A11209,  
896 doi:[10.1029/2008JA013784](https://doi.org/10.1029/2008JA013784).

897 Smirnov, A. G., Berrendorf, M., Shprits, Y. Y., Kronberg, E. A., Allison, H. J., Aseev, N. A., et  
898 al. (2020). Medium energy electron flux in earth's outer radiation belt (MERLIN): A  
899 machine learning model. *Space Weather*, 18,  
900 e2020SW002532. <https://doi.org/10.1029/2020SW002532>

901 Snelling, Jesse M., Jay R. Johnson, Jake Willard, Yosia Nurhan, Jonathan Homan, and Simon  
902 Wing (2020), Information Theoretical Approach to Understanding Flare Waiting Times, *The*  
903 *Astrophysical Journal*, 899, 148, <http://dx.doi.org/10.3847/1538-4357/aba7b9>

904 Spence, H.E., Reeves, G.D., Baker, D.N. et al. (2013), Science Goals and Overview of the  
905 Radiation Belt Storm Probes (RBSP) Energetic Particle, Composition, and Thermal Plasma  
906 (ECT) Suite on NASA's Van Allen Probes Mission. *Space Sci Rev* 179, 311–336,  
907 <https://doi.org/10.1007/s11214-013-0007-5>

908 Stumpo, Mirko; Consolini, Giuseppe; Alberti, Tommaso; Quattrocioni, Virgilio. 2020.  
909 "Measuring Information Coupling between the Solar Wind and the Magnetosphere–  
910 Ionosphere System" *Entropy* 22, no. 3: 276. <https://doi.org/10.3390/e22030276>

911 Summers, D., R. M. Thorne, and F. Xiao (1998), Relativistic theory of wave-particle resonant  
912 diffusion with application to electron acceleration in the magnetosphere, *J. Geophys.*  
913 *Res.*, 103(A9), 20487–20500, doi:[10.1029/98JA01740](https://doi.org/10.1029/98JA01740).

914 Summers, D., Ma, C., Meredith, N. P., Horne, R. B., Thorne, R. M., Heynderickx, D.,  
915 and Anderson, R. R. (2002), Model of the energization of outer-zone electrons by whistler-  
916 mode chorus during the October 9, 1990 geomagnetic storm, *Geophys. Res. Lett.*, 29( 24),  
917 2174, doi:[10.1029/2002GL016039](https://doi.org/10.1029/2002GL016039).

918 Summers, D., B. Ni, and N. P. Meredith (2007), Timescales for radiation belt electron acceleration  
919 and loss due to resonant wave-particle interactions: 1. Theory, *J. Geophys. Res.*, 112,  
920 A04206, doi:[10.1029/2006JA011801](https://doi.org/10.1029/2006JA011801).

921 Tang, C. L., Wang, Y. X., Ni, B., Zhang, J.-C., Reeves, G. D., Su, Z. P., Baker, D. N., Spence, H.  
922 E., Funsten, H. O., and Blake, J. B. (2017a), Radiation belt seed population and its  
923 association with the relativistic electron dynamics: A statistical study, *J. Geophys. Res.*  
924 *Space Physics*, 122, 5261– 5276, doi:[10.1002/2017JA023905](https://doi.org/10.1002/2017JA023905).

925 Takahashi, K., and Ukhorskiy, A. Y. (2007), Solar wind control of Pc5 pulsation power at  
926 geosynchronous orbit, *J. Geophys. Res.*, 112, A11205, doi:[10.1029/2007JA012483](https://doi.org/10.1029/2007JA012483).

927 Thorne, R. M. (2010), Radiation belt dynamics: The importance of wave-particle  
928 interactions, *Geophys. Res. Lett.*, 37, L22107, doi:[10.1029/2010GL044990](https://doi.org/10.1029/2010GL044990)

929 Thorne, R. M., et al. (2013), Rapid local acceleration of relativistic radiation-belt electrons by  
930 magnetospheric chorus, *Nature*, 504(7480), 411–414, doi:10.1038/nature12889.

931 Tsonis, A. A. (2001), Probing the linearity and nonlinearity in the transitions of the atmospheric  
932 circulation, *Nonlinear Processes in Geophysics*, 8, 341–345.

933 Tsyganenko, N. A., and Sitnov, M. I. (2005), Modeling the dynamics of the inner magnetosphere  
934 during strong geomagnetic storms, *J. Geophys. Res.*, 110, A03208,  
935 doi:[10.1029/2004JA010798](https://doi.org/10.1029/2004JA010798)

936 Turner, D. L., and Li, X. (2008), Quantitative forecast of relativistic electron flux at  
937 geosynchronous orbit based on low-energy electron flux, *Space Weather*, 6, S05005,  
938 doi:10.1029/2007SW000354.

939 Turner, D. L., and X. Li (2011), Using spacecraft measurements ahead of Earth in the Parker spiral

940 to improve terrestrial space weather forecasts, *Space Weather*, 9, S01002,  
941 doi:10.1029/2010SW000627

942 Turner, D. L., Y. Shprits, M. Hartinger, and V. Angelopoulos (2012), Explaining sudden losses  
943 of outer radiation belt electrons during geomagnetic storms, *Nat. Phys.*, 8, 208–212,  
944 doi:10.1038/nphys2185.

945 Turner, D. L., et al. (2014a), On the cause and extent of outer radiation belt losses during the 30  
946 September 2012 dropout event, *J. Geophys. Res. Space Physics*, 119, 1530–1540,  
947 doi:[10.1002/2013JA019446](https://doi.org/10.1002/2013JA019446).

948 Turner, D. L., et al. (2014b), Competing source and loss mechanisms due to wave-particle  
949 interactions in Earth's outer radiation belt during the 30 September to 3 October 2012  
950 geomagnetic storm, *J. Geophys. Res. Space Physics*, 119, 1960–1979,  
951 doi:[10.1002/2014JA019770](https://doi.org/10.1002/2014JA019770).

952 Turner, D. L., Kilpua, E. K. J., Hietala, H., Claudepierre, S. G., O'Brien, T. P., Fennell, J. F., et al.  
953 (2019). The response of Earth's electron radiation belts to geomagnetic storms: Statistics  
954 from the Van Allen Probes era including effects from different storm drivers. *Journal of*  
955 *Geophysical Research: Space Physics*, 124, 1013–1034.  
956 <https://doi.org/10.1029/2018JA026066>

957 Turner, D. L., and A. Y. Ukhorskiy (2020), Chapter 1 - Outer radiation belt losses by  
958 magnetopause incursions and outward radial transport: new insight and outstanding  
959 questions from the Van Allen Probes era, in *The dynamic loss of Earth's radiation belts* eds.  
960 Allison N. Jaynes and Maria E. Usanova, Elsevier (2020), pp. 1–20, ISBN 9780128133712,  
961 <https://doi.org/10.1016/B978-0-12-813371-2.00001-9>

962 Ukhorskiy, A. Y., K. Takahashi, B. J. Anderson, and H. Korth (2005), Impact of toroidal ULF

963 waves on the outer radiation belt electrons, *J. Geophys. Res.*, 110, A10202,  
964 doi:[10.1029/2005JA011017](https://doi.org/10.1029/2005JA011017).

965 Ukhorskiy, A. Y., B. J. Anderson, P. C. Brandt, and N. A. Tsyganenko (2006), Storm time  
966 evolution of the outer radiation belt: Transport and losses, *J. Geophys. Res.*, 111, A11S03,  
967 doi:[10.1029/2006JA011690](https://doi.org/10.1029/2006JA011690).

968 Vassiliadis, D., S. F. Fung, and A. J. Klimas (2005), Solar, interplanetary, and magnetospheric  
969 parameters for the radiation belt energetic electron flux, *J. Geophys. Res.*, 110, A04201,  
970 doi:[10.1029/2004JA010443](https://doi.org/10.1029/2004JA010443).

971 Vennerstrøm, S. (1999), Dayside magnetic ULF power at high latitudes: A possible long-term  
972 proxy for the solar wind velocity?, *J. Geophys. Res.*, 104(A5), 10145–10157,  
973 doi:[10.1029/1999JA900015](https://doi.org/10.1029/1999JA900015).

974 Wing, S., Johnson, J. R., Jen, J., Meng, C.-I., Sibeck, D. G., Bechtold, K., Freeman, J., Costello,  
975 K., Balikhin, M., and Takahashi, K. (2005), Kp forecast models, *J. Geophys. Res.*, 110,  
976 A04203, doi:[10.1029/2004JA010500](https://doi.org/10.1029/2004JA010500).

977 Wing, S., J. R. Johnson, C. C. Chaston, M. Echim, C. P. Escoubet, B. Lavraud, C. Lemon, K.  
978 Nykyri, A. Otto, J. Raeder, and C.-P. Wang (2014), Review of solar wind entry into and  
979 transport within the plasma sheet, *Space Science Reviews*, 184, 33 – 86,  
980 doi:[10.1007/s11214-014-0108-9](https://doi.org/10.1007/s11214-014-0108-9)

981 Wing, S., J. R. Johnson, E. Camporeale, and G. D. Reeves (2016), Information theoretical  
982 approach to discovering solar wind drivers of the outer radiation belt, *J. Geophys. Res. Space*  
983 *Physics*, 121, 9378–9399, doi:[10.1002/2016JA022711](https://doi.org/10.1002/2016JA022711)

984 Wing, S., J. Johnson, and A. Vourlidas (2018), Information theoretic approach to discovering  
985 causalities in the solar cycle, *Ap J*, **854**, 85, <https://doi.org/10.3847/1538-4357/aaa8e7>

986 Wing, S, J. R. Johnson (2019), Applications of Information Theory in Solar and Space  
987 Physics, *Entropy*, 21(2):140, <https://doi.org/10.3390/e21020140>

988 Wing, S., P. C. Brandt, D. G. Mitchell, J. R. Johnson, W. S. Kurth and J. D. Menietti (2020),  
989 Periodic Narrowband Radio Wave Emissions and Inward Plasma Transport at Saturn's  
990 Magnetosphere, *Ap J*, 159, 249, 10.3847/1538-3881/ab818d, [https://doi.org/10.3847/1538-](https://doi.org/10.3847/1538-3881/ab818d)  
991 [3881/ab818d](https://doi.org/10.3847/1538-3881/ab818d)

992 Wing, Simon (2021), Untangling the drivers of the radiation belt, Zenodo.  
993 <https://doi.org/10.5281/zenodo.5153481>.

994 Wyner, A. D. (1978), A definition of conditional mutual information for arbitrary ensembles, *Info.*  
995 *and Control*, 38, 51–59.

996 Xiang, Z., Tu, W., Li, X., Ni, B., Morley, S. K., & Baker, D. N. (2017). Understanding the  
997 mechanisms of radiation belt dropouts observed by Van Allen Probes. *Journal of*  
998 *Geophysical Research: Space*  
999 *Physics*, 122, 9858– 9879. <https://doi.org/10.1002/2017JA024487>

1000 Xiang, Z., Tu, W., Ni, B., Henderson, M. G., & Cao, X. (2018). A statistical survey of radiation  
1001 belt dropouts observed by Van Allen Probes. *Geophysical Research Letters*, 45.  
1002 <https://doi.org/10.1029/2018GL078907>

1003 Yokoyama, N., and Kamide, Y. (1997), Statistical nature of geomagnetic storms, *J. Geophys.*  
1004 *Res.*, 102( A7), 14215– 14222, doi:[10.1029/97JA00903](https://doi.org/10.1029/97JA00903)

1005 Zhao, H., Baker, D. N., Jaynes, A. N., Li, X., Elkington, S. R., Kanekal, S. G., Spence, H.  
1006 E., Boyd, A. J., Huang, C.-L., and Forsyth, C. (2017), On the relation between radiation belt  
1007 electrons and solar wind parameters/geomagnetic indices: Dependence on the first adiabatic  
1008 invariant and  $L^*$ , *J. Geophys. Res. Space Physics*, 122, 1624– 1642,

1009      doi:[10.1002/2016JA023658](https://doi.org/10.1002/2016JA023658).

1010

1011

rank	solar wind and magnetospheric parameters	$i_{tr\_max}$	peak $\tau$ (hour)
1	$V_{sw}$	0.12	46
2	SYM-H	0.030	20–60
3	AL	0.020	50–80
4	$P_{dyn}^a$	0.018	7–11
5	IMF $ B ^a$	0.018	50–110
6	IMF $B_z < 0^a$	0.017	50–110
7	$n_{sw}^a$	0.016	7–11
8	IMF $B_y^a$	0.012	0–16
9	Esw	0.012	40–90
10	IMF $B_z > 0$	0.011	0–16
11	$\sigma(\text{IMF B})$	0.0083	0–10

1013

1014

1015 **Table 1.** Ranking of the the solar wind and magnetospheric parameters based on information  
 1016 transfer to radiation belt electron PSD. Parameters 2–11 are calculated from  $\text{CMI}(x \rightarrow \text{PSD} | V_{sw})$   
 1017 where  $x = \text{IMF } |B|, B_z < 0, B_z > 0, B_y, \text{Esw}, \text{ and } \sigma(\text{IMF B})$ . Parameter 1 from  $\text{CMI}(V_{sw} \rightarrow \text{PSD} |$   
 1018  $n_{sw})$ .  $i_{tr\_max} = \text{peak CMI} - \text{mean noise}$  where noise is calculated for surrogate data (see Section  
 1019 4.1).

1020 <sup>a</sup> the response has dual mode: at small  $\tau$  ( $\tau < 15$  hr) the response is electron loss and at large  $\tau$  ( $\tau >$   
 1021 40 hr) the response is electron enhancement. The ranking is based on the larger  $i_{tr\_max}$  of the two  
 1022 responses (see text for explanation).

1023

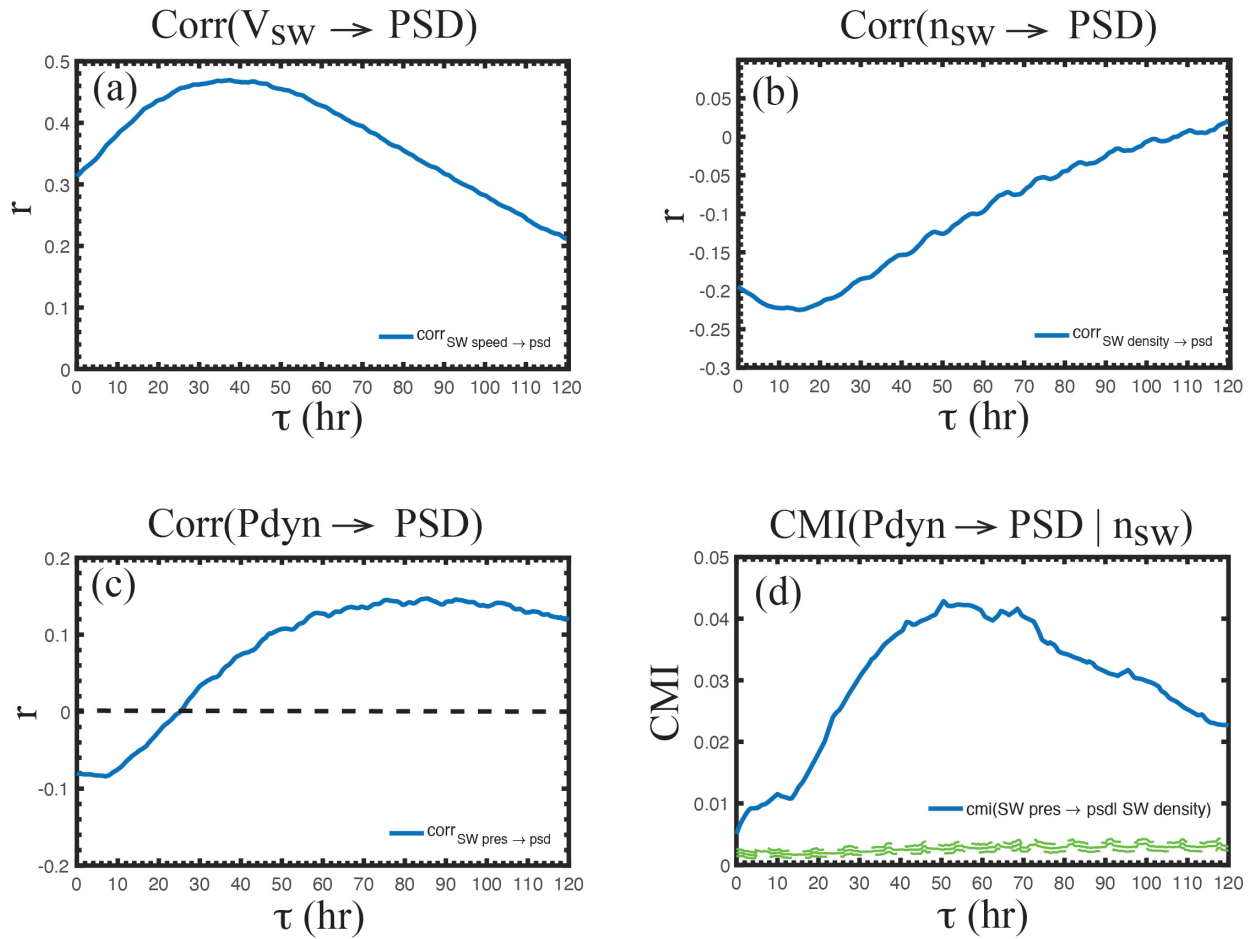
1024

Parameters	Correlation	Peak $\tau$ (hr)	Conditional Mutual Information (CMI)	Peak $\tau$ (hr)
$V_{sw}$	<b>corr(<math>V_{sw} \rightarrow \text{PSD}</math>)</b>	<b>38</b>	<b>CMI(<math>V_{sw} \rightarrow \text{PSD}   n_{sw}</math>)</b>	<b>46</b>
$n_{sw}$	<b>corr(<math>n_{sw} \rightarrow \text{PSD}</math>)</b>	<b>15</b>	<b>CMI(<math>n_{sw} \rightarrow \text{PSD}   V_{sw}</math>)</b>	<b>7</b>
AL	<b>corr(AL <math>\rightarrow</math> PSD)</b>	<b>53</b>	<b>CMI(AL <math>\rightarrow</math> PSD   <math>V_{sw}</math>)</b>	<b>76</b>
SYM-H	<b>corr(SYM-H <math>\rightarrow</math> PSD)</b>	<b>40</b>	<b>CMI(SYM-H <math>\rightarrow</math> PSD   <math>V_{sw}</math>)</b>	<b>55</b>

1025  
1026  
1027  
1028  
1029

**Table 2.** Highlighting the differences between correlation and CMI.  $\tau$  is the radiation belt response lag time.

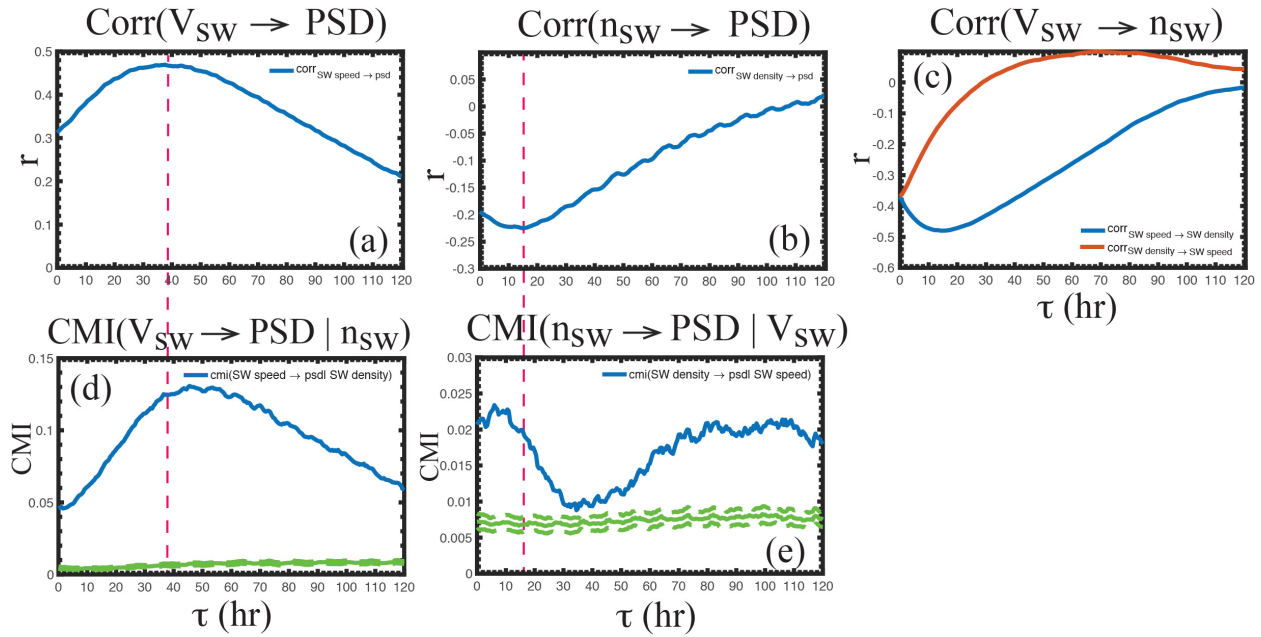
1030  
1031



1032

1033 Figure 1. (a)  $V_{sw}$  positively correlates with radiation belt electron PSD. (b)  $n_{sw}$  negatively  
1034 correlates with PSD. (c) The PSD response to solar wind dynamic pressure ( $P_{dyn}$ ) has two modes:  
1035 at small  $\tau$ ,  $P_{dyn}$  negatively correlates with PSD, similar to  $n_{sw}$  while at large  $\tau$ ,  $P_{dyn}$  positively  
1036 correlates with PSD, similar to  $V_{sw}$ . (d)  $CMI(P_{dyn} \rightarrow PSD | V_{sw})$  is plotted as the blue curve. It  
1037 shows that removing the effect of  $V_{sw}$ , the information transfer from  $P_{dyn}$  to PSD is similar to  $V_{sw}$   
1038 correlation with PSD, as expected. The mean noise and  $3\sigma$  from the noise are plotted as solid and  
1039 dashed green curves, respectively. The peak of the blue curve is  $203\sigma$  above the mean noise and  
1040 hence significant.  
1041

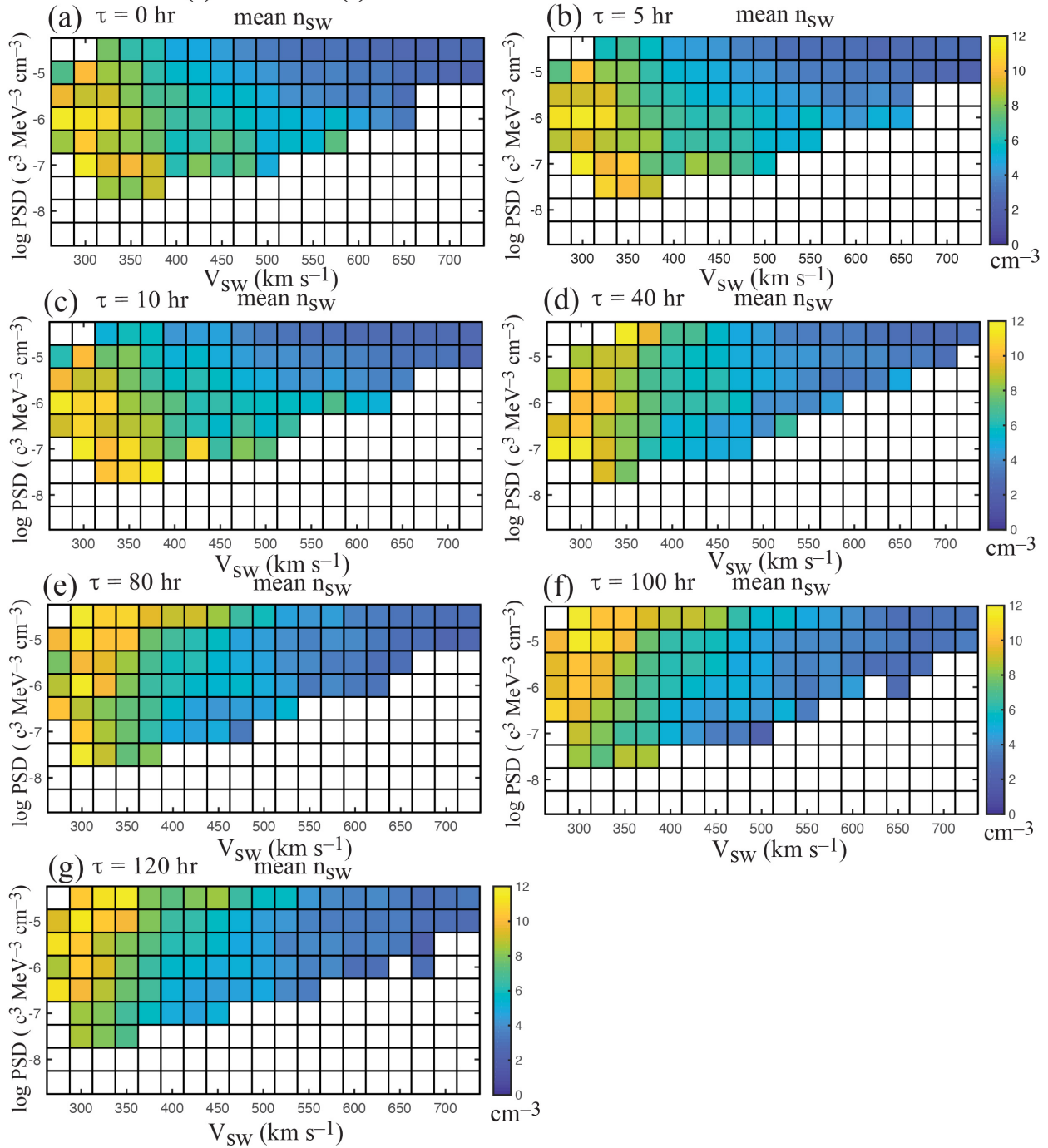
## The effects of $V_{SW}$ and $n_{SW}$ on radiation belt electron psd



1042  
1043

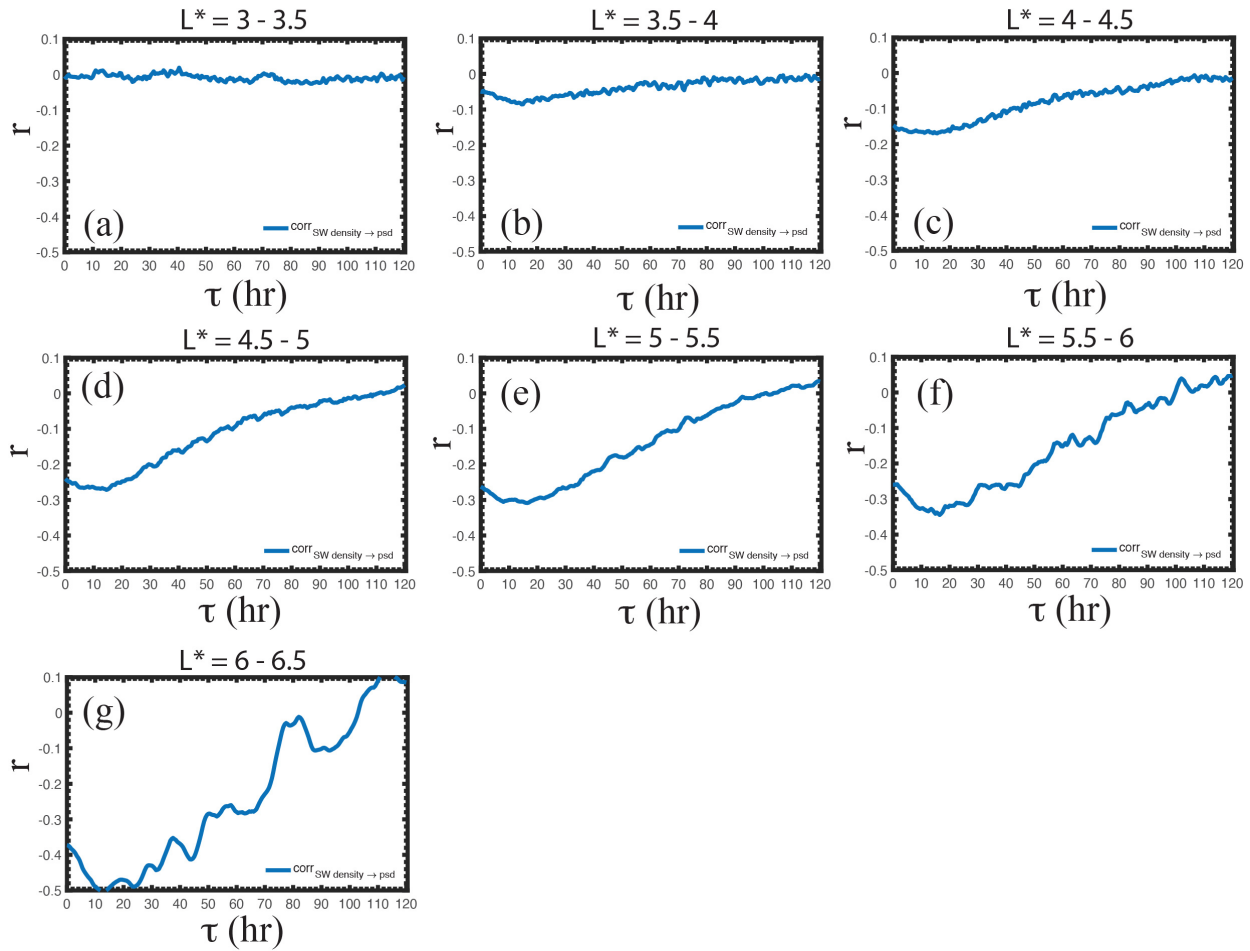
1044 Figure 2. (a)  $V_{SW}$  positively correlates with PSD (same as Figure 1a). (b)  $n_{SW}$  negatively correlates  
1045 with PSD (same as Figure 1b). (c)  $\text{corr}(V_{SW} \rightarrow n_{SW})$  = blue curve and  $\text{corr}(n_{SW} \rightarrow V_{SW})$  = red curve.  
1046 The negative correlation between  $V_{SW}$  and  $n_{SW}$  raises the question that (a) or (b) may be coincidental.  
1047 (d)  $\text{CMI}(V_{SW} \rightarrow \text{PSD} | n_{SW})$  shows that (1) there is still information transfer from  $V_{SW}$  to PSD even  
1048 after the effect of  $n_{SW}$  is removed and (2) removing the effect of  $n_{SW}$  shifts the peak of  $\text{corr}(V_{SW} \rightarrow$   
1049  $\text{PSD})$  to the right. (e)  $\text{CMI}(n_{SW} \rightarrow \text{PSD} | V_{SW})$  shows that (1) there is still information transfer from  
1050  $n_{SW}$  to PSD even after the effect of  $V_{SW}$  is removed and (2) removing the effect of  $V_{SW}$  shifts the peak  
1051 of  $\text{corr}(n_{SW} \rightarrow \text{PSD})$  to the left. The red dashed vertical lines help visualize the shifts of the peaks  
1052 in the correlations.  $\text{CMI}(n_{SW} \rightarrow \text{PSD} | V_{SW})$  has a secondary peak at  $\tau = 80\text{--}120$  hr. The mean noise  
1053 and  $3\sigma$  from the noise are plotted as solid and dashed green curves, respectively.

### $V_{sw}(t)$ vs. $n_{sw}(t)$ vs. radiation belt electron PSD( $t + \tau$ )



1054

1055 Figure 3. (a–g) log PSD( $t + \tau$ ) vs.  $V_{sw}(t)$  vs.  $n_{sw}(t)$  for  $\tau = 0, 5, 10, 40, 80, 100,$  and  $120$  hr,  
 1056 respectively. The color is  $n_{sw}$ . Large  $V_{sw}$  ( $V_{sw} > 450 \text{ km s}^{-1}$ ) corresponds to high PSD. For small  
 1057  $V_{sw}$  ( $V_{sw} < 450 \text{ km s}^{-1}$ ), at small  $\tau$  ( $\tau = 0, 5, 10$  hr),  $n_{sw}$  negatively correlates with PSD, but at large  
 1058  $\tau$  ( $\tau = 80, 100, 120$  hr),  $n_{sw}$  positively correlates with PSD. At  $\tau = 40$ , the correlation is weak.  
 1059 Figure 3 is consistent with  $\text{CMI}(n_{sw} \rightarrow \text{PSD} | V_{sw})$  plotted in Figure 2e.  
 1060

Correlation of  $n_{sw}$  and radiation belt electron PSD as a function of  $L^*$ 

1062

1063

1064

1065

1066

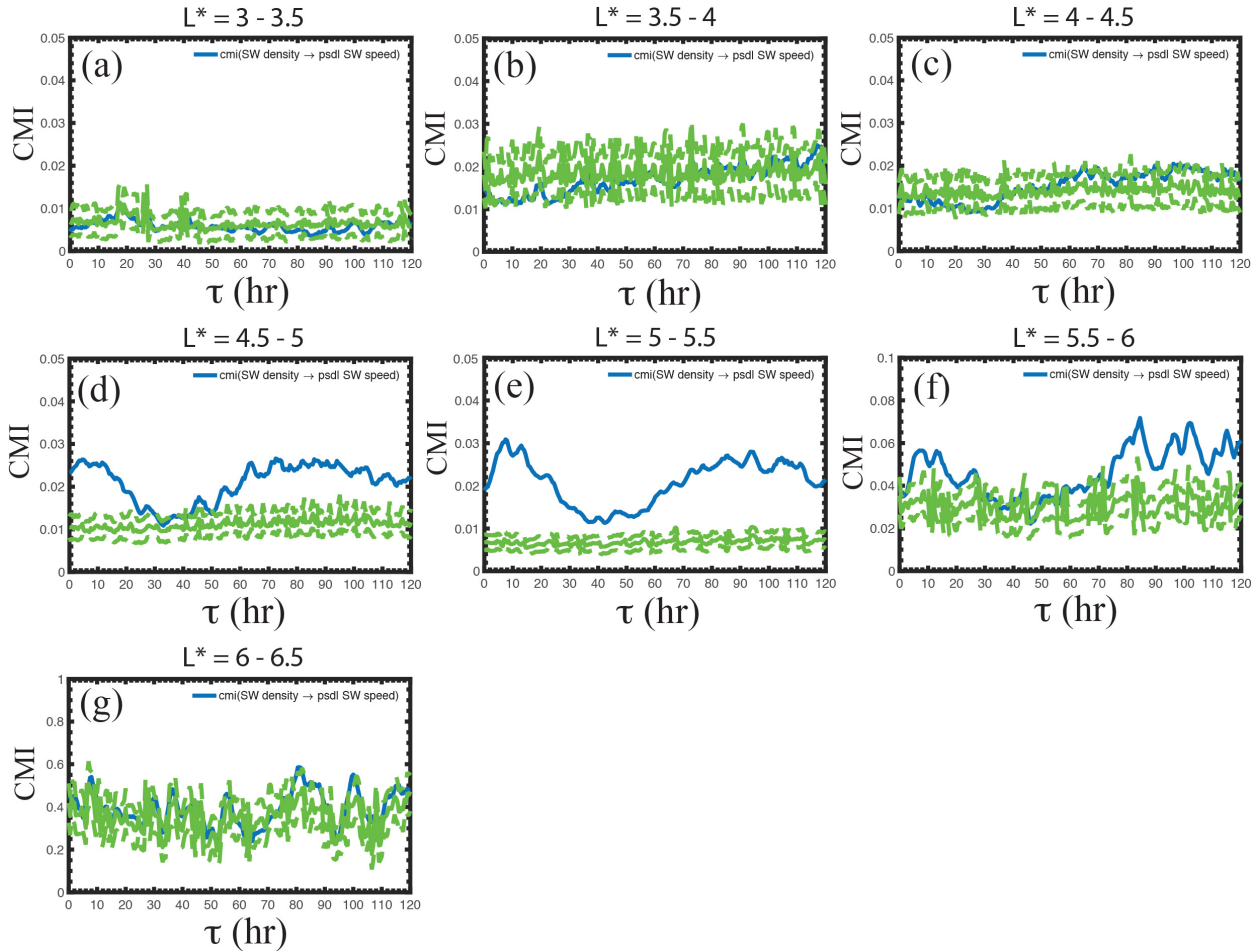
1067

1068

1069

Figure 4.  $\text{corr}(n_{sw} \rightarrow \text{PSD})$  from  $L^* = 3$  to 6.5 in seven bins each with width = 0.5. (a) The correlation is insignificant at  $L^* = 3-3.5$ , but slowly increases with increasing  $L^*$ . (b-g) The correlations are significant ( $p < 0.01$ ) at the minimum  $\tau$  ( $\tau = 15, 16, 17, 17, 17, 13$  hr),  $r = (-0.086, -0.17, -0.27, -0.31, -0.34, -0.50)$ , and  $n = (8,302, 11,481, 17,7891, 27,060, 6,236, 528)$ , respectively.

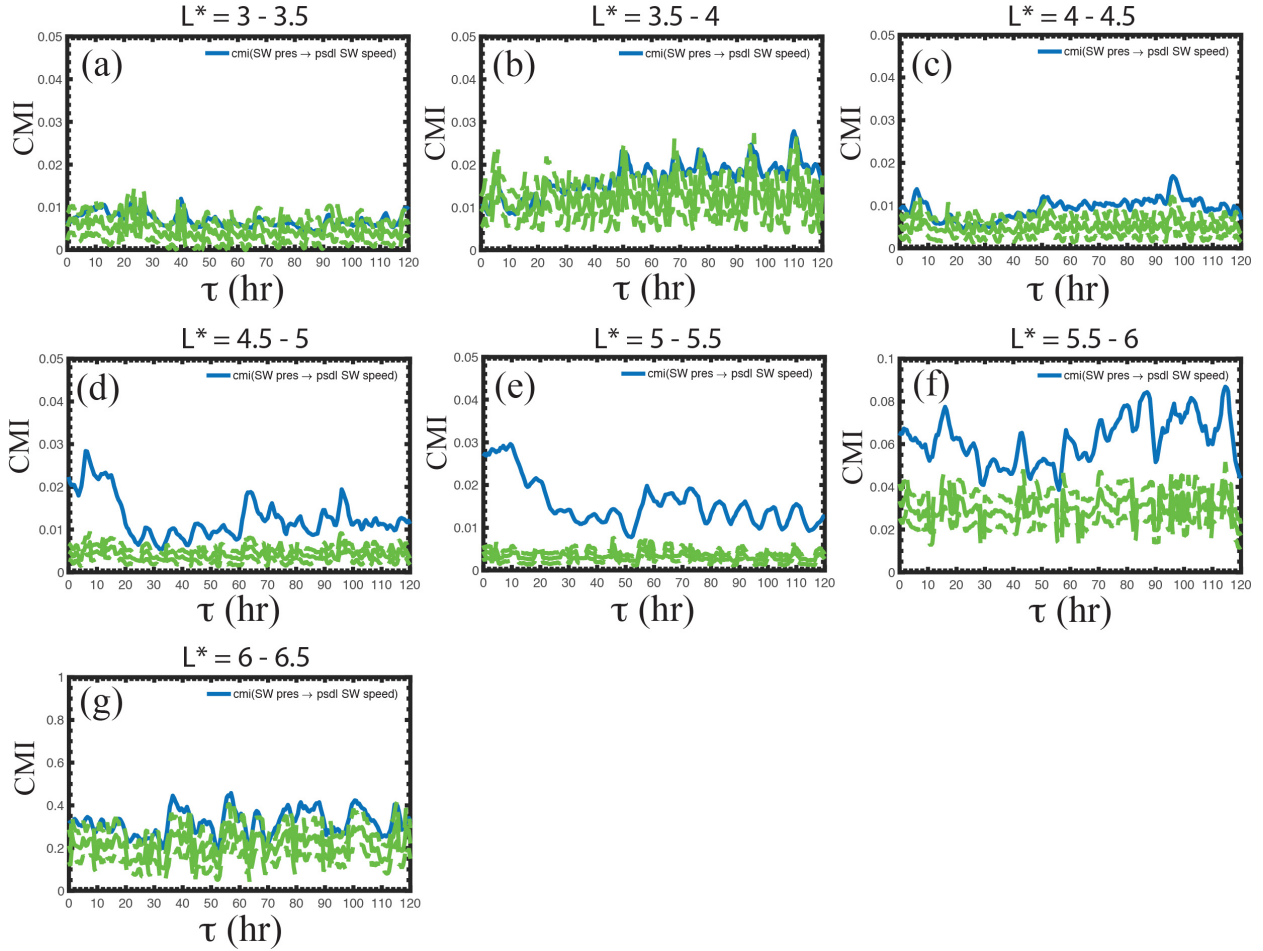
CMI( $n_{sw} \rightarrow \text{PSD} | V_{sw}$ ) as a function of  $L^*$



1070  
 1071 Figure 5. CMI( $n_{sw} \rightarrow \text{PSD} | V_{sw}$ ) from  $L^* = 3$  to 6.5 in seven bins each having width = 0.5. The  
 1072 mean noise and  $3\sigma$  from the noise are plotted as solid and dashed green curves, respectively. (a)  
 1073 The CMI is at the noise level at  $L^* = 3-3.5$ , which is consistent with the correlation in Figure 4a.  
 1074 (b-c) CMI is at the noise level at  $L^* = 3.5-4.5$ , unlike the correlation in Figures 4b and 4c. (d-e)  
 1075 The peak CMI is significant at  $L^* = 4.5-5.5$  and (f) barely significant at  $L^* = 5.5-6$ . (g) The CMI  
 1076 is at the noise level at  $L^* = 6-6.5$  where there is a large variability in PSD at this outermost  $L^*$   
 1077 layer.

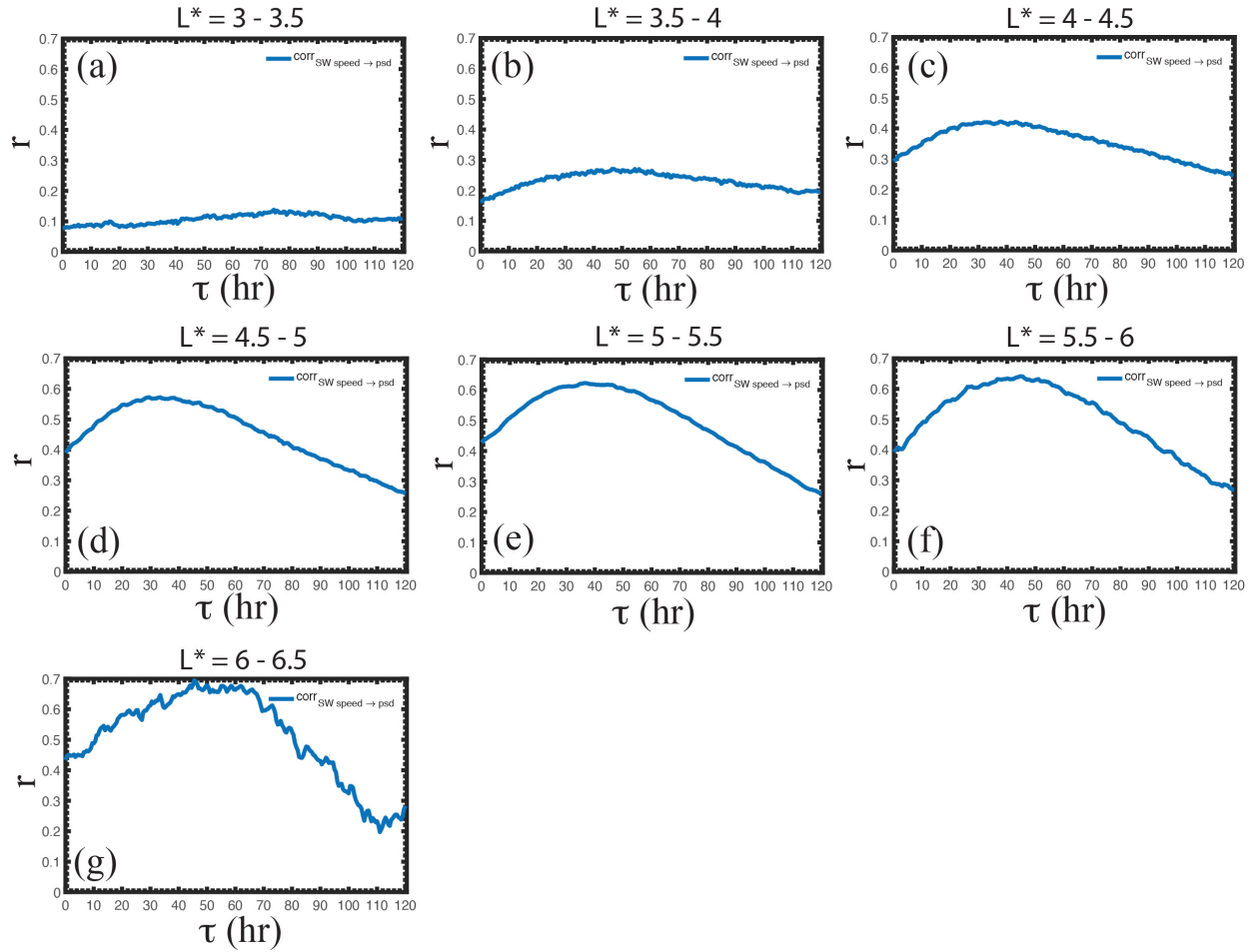
1078  
 1079  
 1080  
 1081  
 1082

CMI( $P_{dyn} \rightarrow PSD | V_{sw}$ ) as a function of  $L^*$



1083  
 1084 Figure 6. CMI( $P_{dyn} \rightarrow PSD | V_{sw}$ ) from  $L^* = 3$  to 6.5 in seven bins in the same format as in Figure  
 1085 5. The mean noise and  $3\sigma$  from the noise are plotted as solid and dashed green curves, respectively.  
 1086 Similar to their counterparts in Figure 5 panels d–f, the primary peak CMIs are significant only at  
 1087  $L^* = 4.5$ –5.5 (d–e) and barely significant at  $L^* = 5.5$ –6. The significances at  $L^* = 4.5$ –6 are higher  
 1088 than their counterparts in Figure 5 panels d–f for CMI( $n_{sw} \rightarrow PSD | V_{sw}$ ), suggesting that  $P_{dyn}$  is the  
 1089 real causal variable rather than  $n_{sw}$ . The opposite is true for the secondary peak, suggesting the  
 1090 causal variable is related more to  $n_{sw}$  rather than  $P_{dyn}$ .

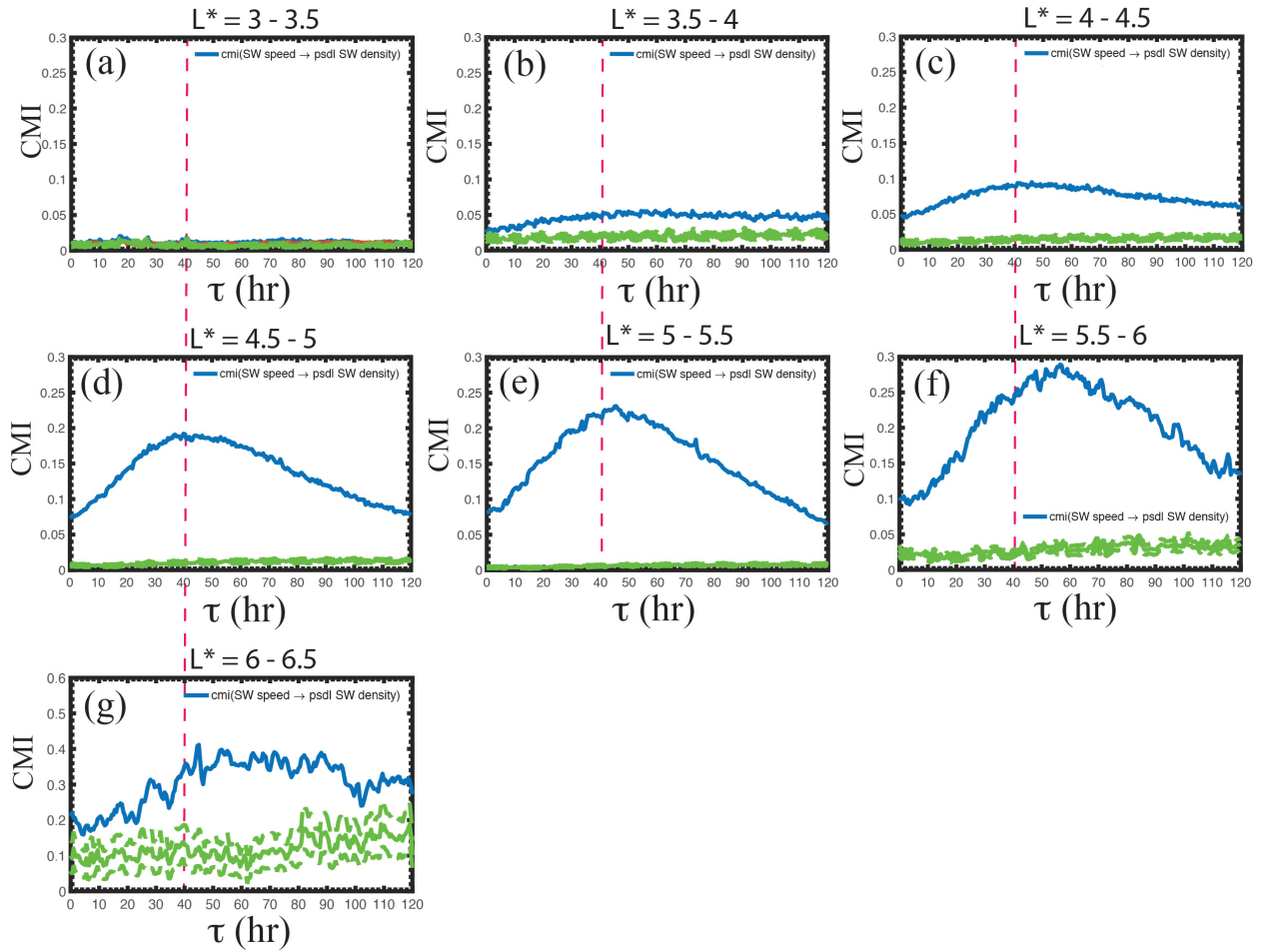
Correlation of  $V_{SW}$  and radiation belt electron PSD as a function of  $L^*$



1091  
1092  
1093  
1094  
1095  
1096  
1097

Figure 7.  $\text{corr}(V_{SW} \rightarrow \text{PSD})$  from  $L^* = 3$  to  $6.5$  in seven bins in the same format as Figure 5. (a–g) The correlations are all significant at  $p < 0.01$  at the maximum  $\tau$  ( $\tau = 40$ – $120$ ,  $30$ – $120$ ,  $38$ ,  $30$ ,  $37$ ,  $45$ ,  $30$ – $90$  hr), ( $r = 0.14, 0.27, 0.42, 0.57, 0.62, 0.64, 0.70$ ) for  $L^* = 3$ – $3.5, 3.5$ – $4, 4$ – $4.5, 4.5$ – $5, 5$ – $5.5, 5.5$ – $6, \text{ and } 6$ – $6.5$ , respectively.

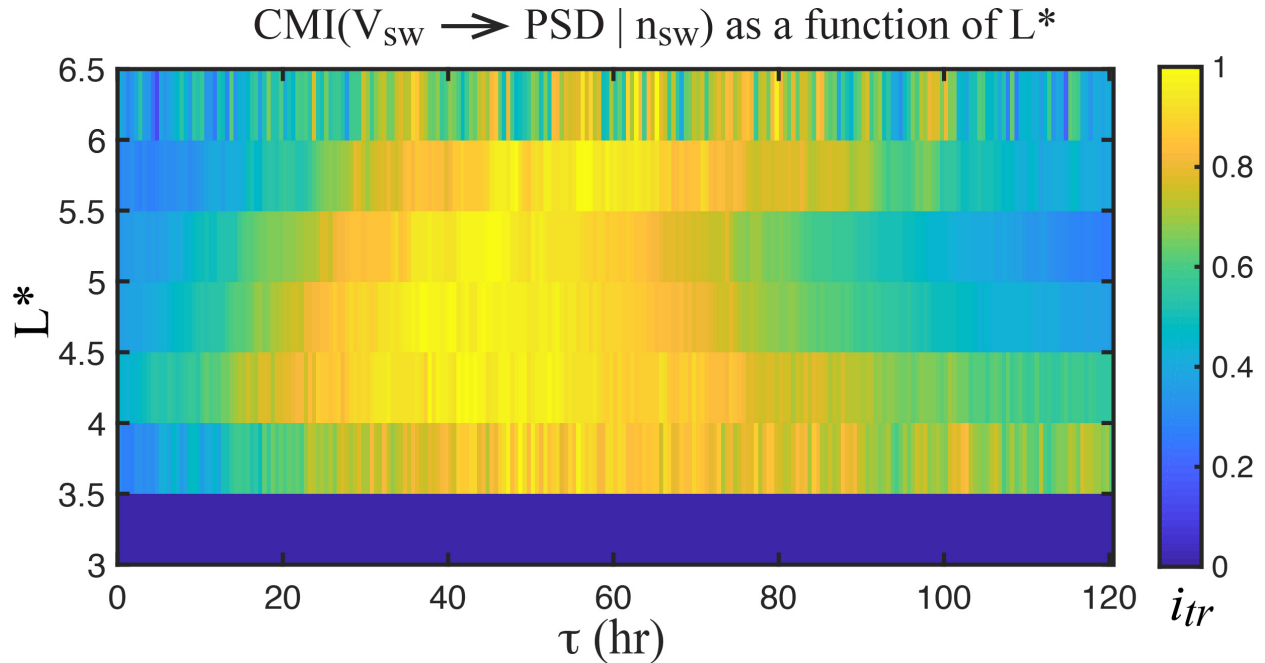
CMI( $V_{sw} \rightarrow \text{PSD} | n_{sw}$ ) as a function of  $L^*$



1098  
1099

1100 Figure 8. CMI( $V_{sw} \rightarrow \text{PSD} | n_{sw}$ ) from  $L^* = 3$  to 6.5 in seven bins in the same format as Figure 5.  
1101 The mean noise and  $3\sigma$  from the noise are plotted as solid and dashed green curves, respectively.  
1102 (a) The CMI is at the noise level at  $L^* = 3-3.5$ , unlike the correlation in Figure 7a. (b-c) At  $L^* =$   
1103  $3.5-4.5$ , the CMI has broad peaks from  $\tau \sim 50$  to 100 hr (or larger in the case  $L^* = 3.5 - 4$ ) and the  
1104 peaks are significant. (d-f) At  $L^* = 4.5-6$ , the CMI peaks are narrower (peak  $\tau = 40, 46, 57$  hr,  
1105 respectively). (g) At  $\tau = 6-6.5$ , the peak broadens again but remains significant.

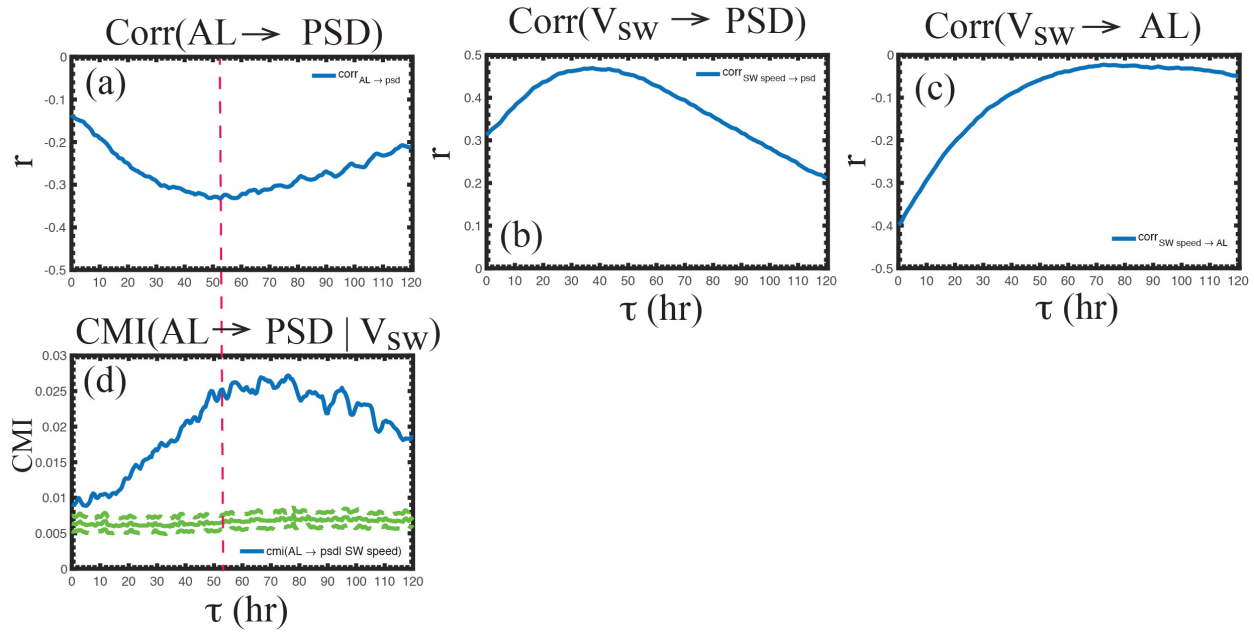
1106  
1107  
1108  
1109  
1110  
1111  
1112



1113  
 1114 Figure 9. The normalized  $i_{tr}$  as a function of  $L^*$  and  $\tau$  where  $i_{tr}$  = the amount of information  
 1115 transferred =  $\text{CMI}(V_{sw} \rightarrow \text{PSD} | n_{sw}) - \text{mean noise}$  (the blue curve subtracted by the solid green  
 1116 curve in Figure 8). The orange and yellow correspond roughly to the top 20% of  $i_{tr}$  in each  $L^*$  bin.  
 1117 The smallest peak  $\tau$  can be found at  $L^* = 4.5 - 5.5$  where  $\tau = 35 - 50$  hr. The peak  $\tau$  broadens and  
 1118 shifts to larger  $\tau$  at higher  $L^*$  ( $t = 45 - 65$  and  $40 - 100$  hr for  $L^* = 5.5 - 6$  and  $6 - 6.5$ , respectively)  
 1119 and lower  $L^*$  ( $\tau = 35 - 55$  and  $45 - 60$  hr for  $L^* = 4 - 4.5$  and  $3.5 - 4$ , respectively). The broadening  
 1120 and shifting of the peak to higher  $\tau$  may suggest outward and inward diffusion from  $L^* = 4.5 - 5.5$ .  
 1121 At  $L^* = 4 - 4.5$ , peak  $\tau$  starts about the same time as that at  $L^* = 4.5 - 5.5$ , which is suggestive of  
 1122 local acceleration at this  $L^*$  band as well.  
 1123

1124

### The effect of AL on radiation belt electron PSD



1125

1126

1127 Figure 10. (a) AL negatively correlates with radiation belt electron PSD. (b)  $V_{sw}$  positively

1128 correlates with PSD (same as Figure 1a). (c)  $V_{sw}$  negatively correlates with AL. Given (b) and (c),

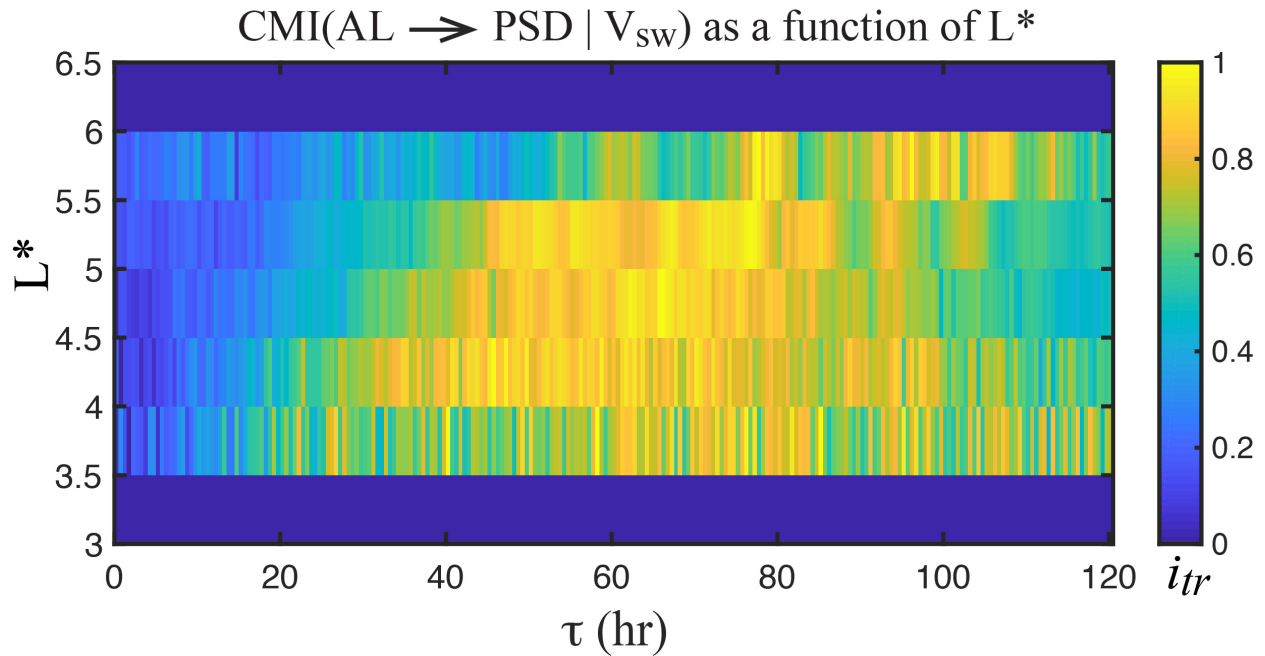
1129 the correlation in (a) may just be coincidental. (d) CMI(AL  $\rightarrow$  PSD |  $V_{sw}$ ) shows that even after

1130 the effect of  $V_{sw}$  has been removed, AL still has an effect on PSD. The mean noise and  $3\sigma$  from

1131 the noise are plotted as solid and dashed green curves, respectively.

1132

1133



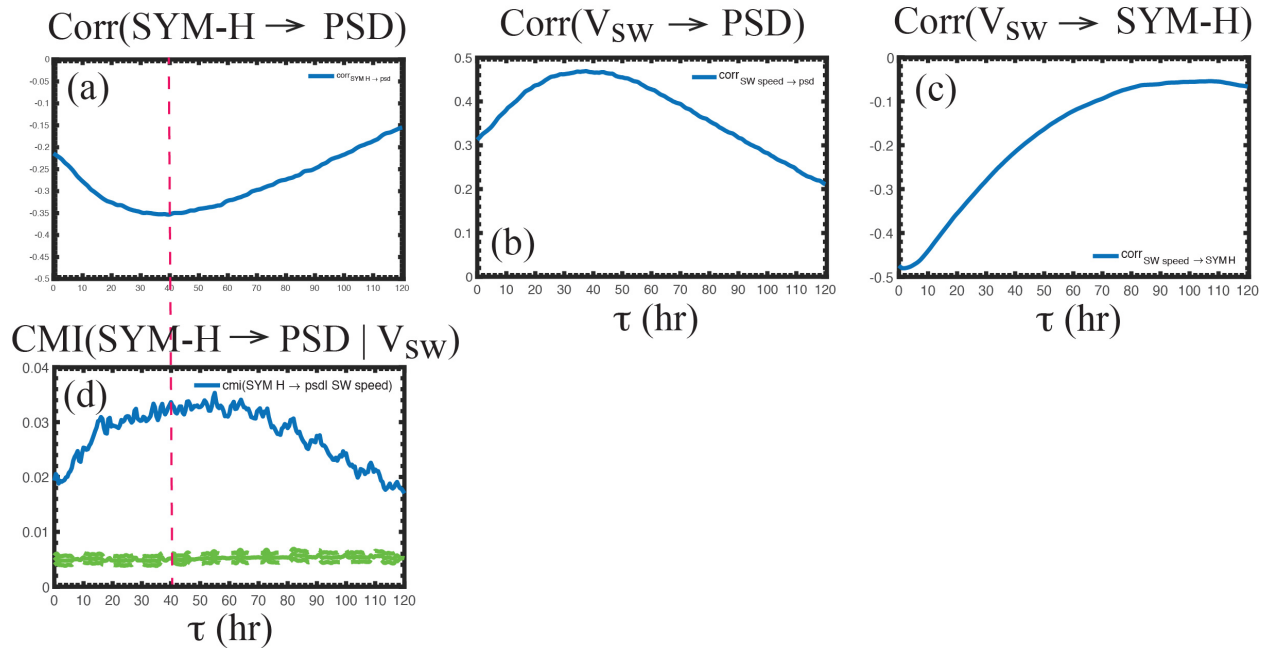
1134

1135 Figure 11. The normalized  $i_{tr}$  as a function of  $L^*$  and  $\tau$  where  $i_{tr}$  = the amount of information  
 1136 transferred =  $\text{CMI}(\text{AL} \rightarrow \text{PSD} | V_{sw}) - \text{mean noise}$  in the same format as Figure 9. The orange and  
 1137 yellow correspond roughly to the top 20% of  $i_{tr}$  in each  $L^*$  bin. The  $i_{tr}$  is at the noise level at  $L^* =$   
 1138 3–4 and 6–6.5. The region with the largest significance is  $L^* = 4.5\text{--}5$  and  $5\text{--}5.5$  with  $\tau = 40\text{--}80$   
 1139 and  $45\text{--}85$  hr, respectively. The peak shifts to higher  $\tau$ ,  $\tau = 75\text{--}100$  hr, at  $L^* = 5.5\text{--}6$ , suggesting  
 1140 outward diffusion from  $L^* = 4.5\text{--}5.5$ . At  $L^* = 4\text{--}4.5$ , the peak is the broad at  $\tau = 35\text{--}80$  hr. Because  
 1141 the peak  $\tau$  starts about the same time as that at  $L^* = 4.5\text{--}5$ , it may suggest local acceleration at this  
 1142  $L^*$ . The slow decay of  $\tau$  suggests inward diffusion or longer lasting wave activity.

1143

1144

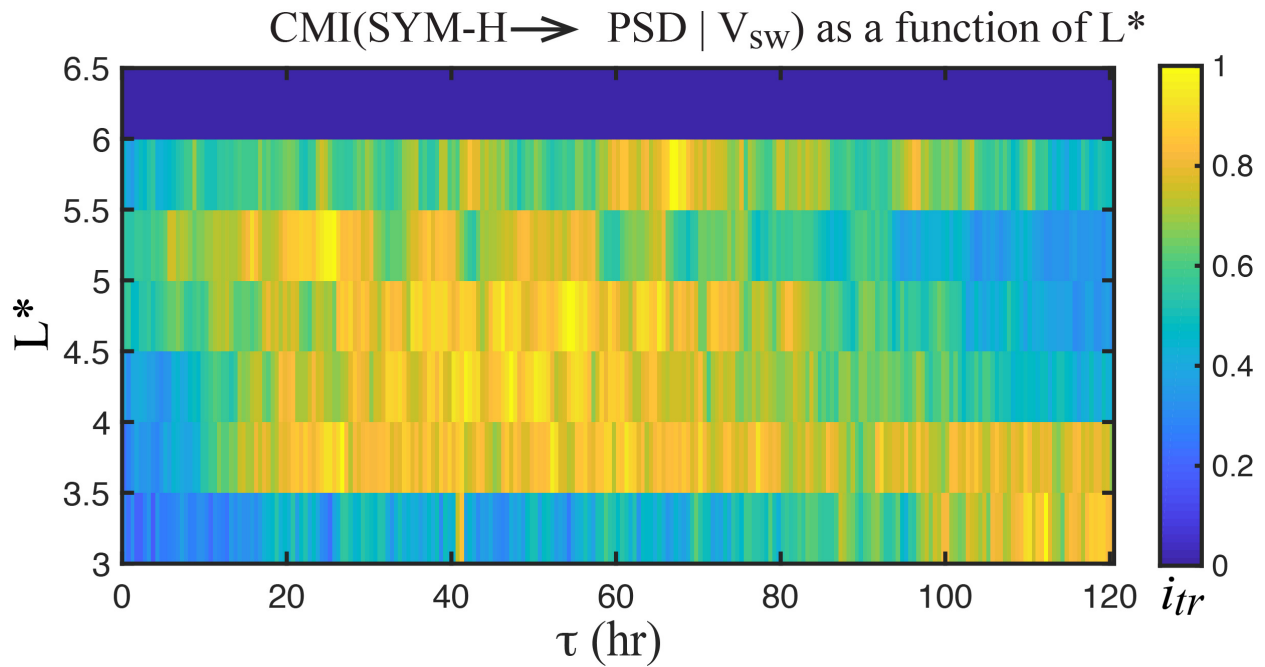
### The effect of Sym-H on radiation belt electron PSD



1145  
1146  
1147  
1148  
1149  
1150  
1151

Figure 12. (a) SYM-H negatively correlates with radiation belt electron PSD. (b)  $V_{sw}$  positively correlates with PSD (same as Figure 1a). (c)  $V_{sw}$  negatively correlates with SYM-H. Given (b) and (c), the correlation in (a) may just be coincidental. (d)  $\text{CMI}(\text{SYM-H} \rightarrow \text{PSD} | V_{sw})$  shows that even after the effect of  $V_{sw}$  has been removed, SYM-H still has an effect on PSD. The mean noise and  $3\sigma$  from the noise are plotted as solid and dashed green curves, respectively.

1152



1153

1154

1155 Figure 13. The normalized  $i_{tr}$  as a function of  $L^*$  and  $\tau$  where  $i_{tr}$  = the amount of information  
 1156 transferred =  $\text{CMI}(\text{SYM-H} \rightarrow \text{PSD} | V_{sw}) - \text{mean noise}$  in the same format as Figure 9. The orange  
 1157 and yellow correspond roughly to the top 20% of  $i_{tr}$  in each  $L^*$  bin. The  $i_{tr}$  is at the noise level at  
 1158  $L^* = 6-6.5$  where there is a large variability in the radiation belt electron PSD. The highest peak  
 1159 significance can be found at  $L^* = 5-5.5$  with  $\tau = 20-55$  hr. The peak broadens and shifts to higher  
 1160  $\tau$ ,  $\tau = 60-75$  hr at  $L^* = 5.5-6$ , suggesting outward diffusion from  $L^* = 5-5.5$ . At  $L^* = 4-4.5$  and  
 1161  $4.5-5$ , the  $i_{tr}$  peaks at  $\tau = 30-60$  and  $30-75$  hr. At  $L^* = 3.5-4$ , the peak is very broad at  $\tau = 20-$   
 1162  $120$  hr, which may suggest local acceleration and inward diffusion from higher  $L^*$ . At  $L^* = 3-$   
 1163  $3.5$ , the  $i_{tr}$  peaks at  $\tau = 110-120$  hr or may be even higher, which may suggest slow diffusion from  
 1164 higher  $L^*$ .

1165